Bin-Emulating Hail Melting in Three-Moment Bulk Microphysics

EDWARD R. MANSELL

NOAA/National Severe Storms Laboratory, Norman, Oklahoma

DANIEL T. DAWSON II

Purdue University, West Lafayette, Indiana

JERRY M. STRAKA

School of Meteorology, University of Oklahoma, Norman, Oklahoma

(Manuscript received 30 September 2019, in final form 29 July 2020)

ABSTRACT: A three-moment bulk microphysics scheme is modified to treat melting in a size-dependent manner that emulates results from a spectral bin scheme. The three-moment bulk framework allows the distribution shape to change and accommodate some direct effects of melting on both the hail and raindrop size distributions. Reflectivity changes and shed raindrop sizes are calculated over discrete size ranges of the hail particle spectrum. Smaller ice particles are treated as melting into drops of the same mass, whereas large particles shed drops as they melt. As small ice particles are lost, the size spectrum naturally becomes narrower and the mean size of small hail can increase. Large hail with a narrow spectrum, however, can decrease in size from melting. A substantial effect is seen on the rain median volume diameter when small drops are shed from large melting hail. The NSSL bulk scheme is compared with bin microphysics in steady-state hail shafts and in a supercell storm case. It is also shown that melting (or any substantial removal of mass) induces gravitational size sorting in bulk microphysics to increase hail size despite the design of the process rates to maintain the mean size of the melting ice. This unintended side effect can be a correct behavior for small hail, but not for large hail with a narrow distribution, when mean hail size should decrease by melting.

KEYWORDS: Hail; Cloud parameterizations; Cloud resolving models

1. Introduction

Cloud physics parameterizations are known to be significant contributors to errors and biases in convection-allowing simulations (e.g., Clark et al. 2012), and many processes contribute to the wide variations noted among different microphysics schemes (e.g., Morrison et al. 2015; Khain et al. 2016; Fan et al. 2017; Han et al. 2019). The melting process is important for cold pool formation and rain characteristics, and has generally been treated relatively simply in bulk microphysics schemes, which predict one or more integral moments (e.g., total mass and particle number) of a prescribed analytical function representing the particle size distribution (PSD). Rasmussen et al. (1984) demonstrated that the characteristics of melting and raindrop shedding depend rather dramatically on the size of the melting ice particle. These behaviors affect hail and raindrop sizes, which in turn drive polarimetric radar features (e.g., Jung et al. 2012; Dawson et al. 2013, 2014; Johnson et al. 2016; Putnam et al. 2017; Snyder et al. 2017). Spectral bin schemes can treat processes dependent on hydrometeor size in a straight-forward manner. Bulk schemes generally use integrations over the prescribed PSD, which precludes a nonanalytic size dependence. Here, we explore the use of a three-moment bulk scheme with integrations over a few specific size ranges in a ''quasi-bin'' or ''bin-emulating'' approach to the problem that retains computational efficiency compared to a full bin scheme.

Most multimoment bulk microphysics schemes predict the total mass (third moment in diameter), number concentration (zeroth moment), and, for three-moment schemes, reflectivity (sixth moment) (e.g., Milbrandt and Yau 2005a; Dawson et al. 2014). Other choices are possible, however, as shown for two-moment schemes by Straka et al. (2005) and in two- and three-moment schemes by Milbrandt and McTaggert-Cowan (2010) (for sedimentation). More sophisticated configurations are possible as in Farley and Orville (1986) and Johnson et al. (1993), who used a spectral bin method for hail combined with bulk physics for the other species. Another method is the hybrid-bin approach, where microphysics rates are found by transforming the bulk distributions into temporary spectral bin classes or by using lookup tables of bin calculations to compute moment rates (e.g., Feingold et al. 1998; Morrison 2012; Loftus et al. 2014; Kudzotsa et al. 2016; Paukert et al. 2019).

The present work builds upon Milbrandt and Yau (2005b), Mansell et al. (2010), and Dawson et al. (2014) with the use of a three-moment bulk scheme and its key advantage (over the two-moment bulk scheme) of allowing the shape parameter α to vary within the assumed gamma function size distribution in diameter:

$$n_x(D) = \frac{N_x D^{\alpha_x}}{D_{n,x}^{1+\alpha_x}\Gamma(1+\alpha_x)} \exp(-D/D_{n,x}), \quad (1)$$

Corresponding author: Edward Mansell, ted.mansell@noaa.gov

DOI: 10.1175/JAS-D-19-0268.1

where N_x is the total number concentration of hydrometeor species x, Γ is the complete gamma function, and D_n is the characteristic diameter, which is the reciprocal of the commonly used slope parameter λ:

$$D_{n,x} \equiv \frac{1}{\lambda_x} = \left[\frac{q_x \rho_{\text{air}} \Gamma(1+\alpha_x)}{c_x N_x \Gamma(1+\alpha_x+d_x)}\right]^{1/d_x}, \tag{2}$$

where q_x is the mass mixing ratio, and c_x and d_x define the mass–diameter relationship (Table 1). The effective width of the distribution can range from very wide (e.g., $\alpha \leq 0$) to quite narrow (e.g., $\alpha > 6$). A primary process that can cause narrowing of the spectrum is gravitational size sorting (Milbrandt and Yau 2005a; Mansell 2010; Milbrandt and McTaggert-Cowan 2010; Dawson et al. 2014; Loftus et al. 2014), where the downward leading edge of a 1D precipitation shaft is led by the largest (i.e., fastest-falling) particles. In a three-moment scheme, the leading edge develops a narrower distribution as the large particles outrun the smaller ones before reaching the ground.

In addition to transient size sorting (e.g., as in Milbrandt and Yau 2005a; Mansell 2010) steady-state size sorting can be achieved by maintaining a constant source aloft in the presence of horizontal wind, which maintains a vertical size sorting "leading edge" profile by the relative horizontal advection of mass (e.g., Kumjian and Ryzhkov 2012; Dawson et al. 2014, 2015). Melting can have a similar effect in a steady 1D hail shaft, as will be demonstrated below, by removing mass from the hydrometeors, much like horizontal advection.

In Milbrandt and Yau (2005b) and Dawson et al. (2014), the microphysical reflectivity moment rates for a given processes (e.g., accretion) were diagnosed from the rates for number concentration and mass. The reflectivity rate calculation assumed that the process had minimal effect on the shape parameter. For some processes, however, it can be relatively straightforward to integrate the reflectivity change directly, which allows the shape parameter to be directly affected, as in the three-moment warm rain scheme of Naumann and Seifert (2016). Melting of graupel or hail, for example, should remove smaller particles more rapidly from the distribution than larger particles and lead to a narrower distribution. (At least in the case here where liquid fraction on ice is not predicted, which requires immediate transfer of meltwater to the rain category.)

In this paper, melting of graupel and hail as described by Rasmussen et al. (1984) is treated by integrations over specific size ranges in a bin-emulating approach, which has similarities to the ice parameterization of Morrison and Milbrandt (2015), which defined ice particle properties that varied over parts of the size spectrum. The method is described and then applied first to a simple, steady-state 1D hail shaft and second to a supercell storm simulation. Results are then tied back to Dawson et al. (2014), who related gravitational size sorting of hail and rain to simulated polarimetric radar variables.

2. Model and microphysics

a. Model

The Collaborative Model for Multiscale Atmospheric Simulation (COMMAS; Wicker and Wilhelmson 1995; Coniglio et al. 2006; Mansell et al. 2010) is used for all experiments. COMMAS uses the Klemp and Wilhelmson (1978) atmospheric equation set, using the same strategy of integrating sound waves on a split time step. Time integration uses a third-order Runge–Kutta scheme (RK3; Wicker and Skamarock 2002). Advection of both scalars and momentum typically uses a fifth-order upwind-biased stencil for the first two steps of the RK3, and for the third step either the same stencil or a fifth-, seventh-, or ninth-order weighted essentially nonoscillatory (WENO) scheme (Balsara and Shu 2000). Hydrometeor sedimentation uses a forward-in-time first-order upwind scheme (Mansell 2010), which can take multiple substeps depending on the fall speed Courant number. In full 3D simulations, the surface is treated as free-slip, and radiative lateral boundary conditions are employed.

b. Bulk NSSL scheme: "Control–bulk" and "bin–bulk"

The bulk microphysics scheme used here is the multimoment National Severe Storms Laboratory (NSSL) parameterization (Mansell et al. 2010; Ziegler 1985). The two-moment version of the scheme is essentially the same as in the Weather Research and Forecasting (WRF) Model and Cloud Model 1 (CM1; Bryan and Fritsch 2002). It has six hydrometeor categories (cloud droplets, rain, cloud ice, snow, graupel, and hail), for which mass and number concentration are predicted. The reflectivity moment (sixth moment in diameter) can be predicted for fast-falling species (rain, graupel, and hail) (Dawson et al. 2014). The PSD shape parameters α_x are found by an iterative method (appendix C). The average particle density can be predicted for graupel and hail by tracking the total particle volume (Mansell et al. 2010; Mansell and Ziegler 2013). Note that ice density prediction is only used here for the supercell simulation, and constant values are used for the steady-state hail-shaft experiments for simplicity and comparison with the spectral bin scheme. Cloud condensation nuclei (CCN) number concentration is also predicted (e.g., Mansell and Ziegler 2013). For the experiments herein, graupel and hail do not collect liquid at temperatures greater than 0°C, although the collection rate is calculated for use in the melting equation in the control simulations. The only explicit rain breakup in the bulk scheme is the application of a limit of 6 mm applied to the mass-weighted diameter. An implicit breakup is applied in the form of gradually reducing rain self-collection as the mean-mass rain diameter increases toward 2 mm and is turned off for larger sizes. The unmodified bulk scheme will be referred to as "control–bulk" and the new version with bin-emulating melting will be "bin–bulk."

The NSSL scheme's hail category is designed to emulate a "true" hail that arises from rapid (wet) riming growth of dense graupel (Mansell et al. 2010). This differs from the more common categorization of graupel and hail species by density in both bulk (e.g., Ferrier 1994; Milbrandt and Yau 2005b; Loftus et al. 2014) and spectral bin schemes such as Khain and Sednev (1995) and the Takahashi bin scheme used herein (Takahashi 1976a), where the hail category includes smaller frozen drops. The predicted bulk particle density allows graupel to have characteristics ranging from low density graupel (from rimed ice or snow) to high-density frozen drops. Frozen raindrops are therefore converted to high-density

TABLE 1. Symbols used in the text.

Symbol	Meaning/reference	Value	SI units
a_x	Factor in fall speed relationship, $v_x = a_x D^{b_x}$ (Mansell et al. 2010)		$\mathrm{m}^{(1-b_x)}\mathrm{s}^{-1}$
a_r	Factor in rain fall speed relationship, $\gamma a_r[1 - \exp(-f_r D)]$ (Dawson et al. 2014)	10	$\mathrm{m}^{(1-b_x)}\mathrm{s}^{-1}$
a_h	Ventilation coefficient for heat, $a_h = c_1 + c_2 \mathrm{Sc}^{1/3}\mathrm{Re}^{1/2}$		
a_m	Ventilation coefficient for mass, $a_m = c_1 + c_2 \mathrm{Pr}^{1/3}\mathrm{Re}^{1/2}$		
b_x	Exponent in fall speed relationship		
c_p	Specific heat of dry air at constant pressure	1004	$\mathrm{J\,kg^{-1}\,K^{-1}}$
c_1	Constant in ventilation term [Beard and Pruppacher 1971, Eqs. (8) and (9)]	0.78 or 1.0	
c_2	Constant in ventilation term [Beard and Pruppacher 1971, Eqs. (8) and (9)]	0.308 or 0.108	
c_x	Coefficient in mass–diameter relationship $m_x = c_x D^{d_x}$		$\mathrm{kg\ m^{-}}^{d_x}$
C_D	Drag coefficient (Mansell et al. 2010)	0.45–1.0	
C_w	Water heat capacity, $4243 + 0.3471T^2$		
d or D	Particle diameter		m
d_x	Exponent in mass–diameter relationship, $m_x = c_x D^{d_x}$		
D_{0r}	Rain median volume diameter $= (3.67 + \alpha_r)D_{n,r}$		m
D_{m1}	Diameter below which no shedding occurs (D_{crit})	9	mm
D_{m2}	Diameter between shed drops of 4.5 and 3.0 mm	16	mm
D_{m3}	Diameter above which shedding produces 1.5 mm drops	19	mm
$D_{n,x}$	Characteristic diameter of species x ($1/\lambda_x$)		m
D_{MxMas}	Diameter of maximum mass (also the area-weighted diameter)		mm
$\overline{D}_x$	Mean-mass diameter of species x		mm
f_r	Exponential factor in rain fall speed relationship (Dawson et al. 2014)	516.575	$\mathrm{m^{-1}}$
g	Acceleration due to Earth's gravity	9.81	$\mathrm{m\,s^{-2}}$
K_a	Thermal conductivity of air, $K_a = \eta K_{a,0}/K_{a,1}$ (Straka and Mansell 2005)		$\mathrm{J\,m^{-1}\,s^{-1}\,K^{-1}}$
$K_{a,0}$	Thermal conductivity coefficient	2.43×10^{-2}	
$K_{a,1}$	Thermal conductivity coefficient	1.718×10^{-5}	
L_f	Heat of fusion (Straka and Mansell 2005)		$\mathrm{J\,kg^{-1}}$
L_v	Heat of vaporization (Straka and Mansell 2005)		$\mathrm{J\,kg^{-1}}$
$n(x)$	Number of particles in mass bin x		$\mathrm{cm^{-3}}$
N_x	Total number concentration of hydrometeor category x		$\mathrm{m^{-3}}$
q_x	Mass mixing ratio of water substance category x		$\mathrm{kg\,kg^{-1}}$
q_v	Mass mixing ratio of water vapor x		$\mathrm{kg\,kg^{-1}}$
$q_{v,s}$	Saturation water vapor mixing ratio (with respect to liquid)		$\mathrm{kg\,kg^{-1}}$
$q_{v,s,0}$	Saturation water vapor mixing ratio (with respect to liquid) at $T = 273.15$ K		$\mathrm{kg\,kg^{-1}}$
Re	Reynolds number, $\mathrm{Re} = 2rv/\nu = Dv_t/\nu$ (for sphere)		
Sc	Schmidt number, $\mathrm{Sc} = \nu/\Psi$		
T	Temperature		K
v_{crit}	Critical drop freezing volume		$\mathrm{cm^3}$
$v_{\mathrm{tx}}(D)$	Terminal fall speed of particle of species x with diameter D		$\mathrm{m\,s^{-1}}$
Z_x	Reflectivity moment of hydrometeor category x		$\mathrm{m^{-3}}$
α	Shape parameter in the gamma size distribution function		
α_{min}	Minimum shape parameter for rate equations (graupel/hail/rain) (can be set as low as −0.95)	0	
α_{max}	Maximum shape parameter for rate equations (graupel/hail/rain)	15	
α_{mxmlt}	Limiting graupel/hail shape parameter in bin–bulk melting	14.5	
η	Dynamic viscosity of air ($\rho_{\mathrm{air}}\nu$)		$\mathrm{m^{-2}\,s^{-1}}$
γ	Fall speed factor ($b = 1/2$ for bulk, 0.39 for bin ice crystals)	$(\rho_o/\rho_{\mathrm{air}})^b$	
λ_x	Slope parameter in the gamma size distribution function		
ν	Kinematic viscosity of air (Straka and Mansell 2005)		$\mathrm{kg\,m^{-2}\,s^{-4}}$
ρ_{air}	Air density		$\mathrm{kg\,m^{-3}}$
ρ_o	Reference air density	1.225	$\mathrm{kg\,m^{-3}}$
Ψ	Water vapor diffusivity (Straka and Mansell 2005)		$\mathrm{m^2\,s^{-1}}$

graupel instead of hail, which helps avoid undesirable dilution of the hail size aloft (Milbrandt and Yau 2006).

c. *Takahashi spectral bin scheme ("bin scheme")*

The Takahashi (1976a) spectral bin microphysics scheme was employed to compare melting-related results with the NSSL bulk scheme. The code was adapted from Takahashi and Shimura (2004) as described in appendix B. Briefly, as in Fig. B1, there are 34 mass bins for liquid particles (cloud droplets, drizzle, rain), 45 bins each for low-density rimed ice (graupel, $\rho_g = 300\,\mathrm{kg\,m^{-3}}$) and high-density hail/frozen drops ($\rho_h = 900\,\mathrm{kg\,m^{-3}}$). Ice crystals are predicted on 2D grid of

radius (21 bins) and thickness (5 bins), where radius is affected by deposition, sublimation, aggregation, and melting, and thickness changes via riming growth. For the 1D sedimentation tests, only melting is active, and this process is sufficiently similar that the bin and bulk schemes can be reasonably directly compared. For 3D simulations with all processes active, however, spectral bin schemes are not necessarily more reliable than bulk microphysics as shown, for example, by Xue et al. (2017), but can be capable of producing comparable forecast solutions (e.g., Fan et al. 2017). The Takahashi scheme will interchangeably be referred to as simply the bin scheme.

One of the most important upgrades to the Takahashi scheme was the addition of incremental melting rates, which replaces the original method of instantaneous complete particle melting at specified temperatures. The bin scheme only calculates ice–liquid collection when $T < 0$°C. A relatively simple collisional drop breakup parameterization (Young 1975) was also added. In the sedimentation tests, liquid drop–drop interactions (coalescence and collisional breakup) were deactivated in the bin scheme (except where otherwise specified) for better direct comparison with the bulk results. For comparisons with the three-moment bulk scheme, gamma function shape parameters are estimated from the bin distribution by summing the appropriate moments and then using the same iterative solution method as in the bulk scheme (appendix C).

d. Bin-emulating melting

This section describes the details of implementation of a parameterization of melting based on the results of Rasmussen et al. (1984), who documented a range of distinct melting modes of ice spheres suspended in a wind tunnel. Figure 1 summarizes their results as used in the parameterization here. In their study, ice spheres with initial diameters from 3 to 20 mm were suspended in airflow. Larger spheres melted and then shed part of the meltwater until the particle (ice core plus liquid shell) reached a diameter of about 9 mm (D_{m1} in Fig. 1). No shedding occurred for sizes less than about 9 mm, and internal circulations appeared as the water fraction increased with further melting. Shedding from larger particles ($D > D_{m3}$) could take the form of small drops (about 1.5 mm diameter) while intermediate ice particles (from D_{m1} to D_{m3}) were seen to shed larger drops (3–4.5 mm). The hail spectrum is divided into four ranges: (i) $D \le D_{m1}$ with no shedding, (ii) $D_{m1} < D \le D_{m2}$ with larger drop (4.5 mm) shedding, (iii) $D_{m2} < D \le D_{m3}$ with medium drop (3 mm) shedding, and (iv) $D > D_{m3}$ with shedding of smaller drops (1.5 mm). The hail size ranges were also expressed in terms of Reynolds numbers, which could perhaps be more accurately applied at higher altitude, but the diameter ranges are used here for simplicity of integration. The Rasmussen et al. (1984) experiment used highly idealized spherical ice that was loosely tethered horizontally to prevent tumbling, although some spinning was possible, whereas real hailstones can take a variety of shapes and often have irregular lobed structures and gyrations. Therefore, the results may not capture the considerable uncertainty in real situations, such as with tumbling (e.g., Knight and Knight 1970) or gyrations

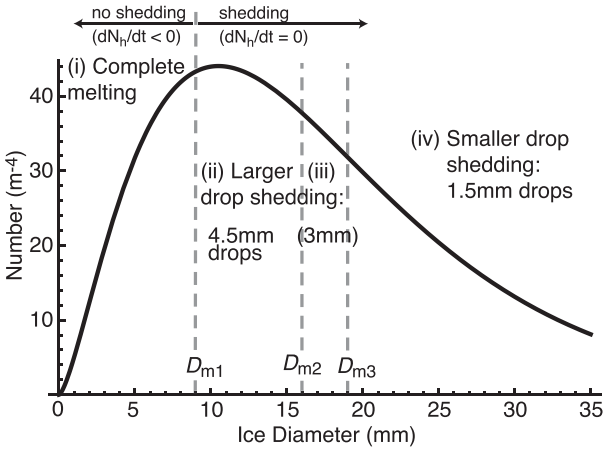

FIG. 1. Illustration of melting regimes based on Rasmussen et al. (1984), where $D_{m1} = 9$ mm, $D_{m2} = 16$ mm, and $D_{m3} = 19$ mm. Complete melting reduces the hail number concentration ($dN_h/dt < 0$) in region (i), but shedding only reduces particle mass and not the particle number ($dN_h/dt = 0$) in regions (ii)–(iv). The curve represents an arbitrary hail size distribution with a total number concentration $N = 1\ \mathrm{m}^{-3}$, characteristic diameter $D_n = 7$ mm, and shape parameter $\alpha = 1.5$.

[e.g., Lesins and List (1986), although they examined shedding during wet growth rather than melting]. Rasmussen et al. (1984) also documented collisions between drops and melting ice that caused ejection of smaller drops, but this process is not parameterized here. Sensitivity of the melting effects to the value of D_{m1} is tested by varying it over a range from 7 to 11 mm in a 1D hail-shaft experiment.

Following Wisner et al. (1972), using Reynolds number $\mathrm{Re} = v_{tx}D/\nu$ but neglecting accretion of liquid particles, the mass melting rate for an ice particle of diameter D is given by

$$\left.\frac{\partial m_x(D)}{\partial t}\right|_{\text{melting}} = -\left[c_1 + c_2 \mathrm{Sc}^{1/3}\left(\frac{v_{tx}D}{\nu}\right)^{1/2}\right] D\rho_{\text{air}} f_{\text{mlt}}, \quad (3)$$

where the bracketed term is the ventilation factor (Beard and Pruppacher 1971), and the particle fall speed is v_{tx}. (See Table 1 for definitions of symbols.) Fall speeds for graupel and hail are parameterized as power law: $v_{tx} = \gamma a_x D^{b_x}$, where x refers to a given species of ice (e.g., graupel or hail), and γ is an adjustment for air density. The f_{mlt} factor contains the rates of heat conduction and latent heat of vaporization as

$$f_{\text{mlt}} = \frac{2\pi}{L_f}\left[L_v \Psi(q_{v,s,0} - q_v) - \frac{K_a}{\rho_{\text{air}}}(T - 273.15)\right] \quad (4)$$

(Mason 1956).

The total ice mixing ratio melting rate can then be found by integrating over the entire size distribution as

$$\left.\frac{\partial q_x}{\partial t}\right|_{\text{mlt},(0,\infty)} = \frac{1}{\rho_{\text{air}}}\int_0^\infty \frac{\partial m_x(D)}{\partial t} n_x(D)\, dD \quad (5)$$

$$= -N_x D_{n,x} f_{\text{mlt}} \text{xvent}, \quad (6)$$

where

$$\text{xvent} = c_1(1+\alpha_x) + c_2 \frac{\Gamma(5/2+\alpha_x+b_x/2)}{\Gamma(1+\alpha_x)} \text{Sc}^{1/3}(a_x\gamma/\nu)^{1/2} D_{n,x}^{(1+b_x)/2}. \tag{7}$$

The melting over the range (D_{m1}, ∞) introduces the upper incomplete gamma function $\Gamma(x, y)$[1] in the "xvent" term

$$\left.\frac{\partial q_x}{\partial t}\right|_{\text{mlt},(D_{\text{m1}},\infty)} = \frac{1}{\rho_{\text{air}}} \int_{D_{\text{m1}}}^{\infty} \frac{\partial m_x(D)}{\partial t} n_x(D)\, dD \tag{8}$$

$$= -N_x D_{n,x} f_{\text{mlt}} \text{xvent}_{D_{\text{m1}}}, \tag{9}$$

where

$$\text{xvent}_{D_{\text{m1}}} = \frac{c_1\Gamma(2+\alpha_x, D_{\text{m1}}/D_{n,x}) + c_2\Gamma(5/2+\alpha_x+b_x/2, D_{\text{m1}}/D_{n,x})\text{Sc}^{1/3}(a_x\gamma/\nu)^{1/2} D_{n,x}^{(1+b_x)/2}}{\Gamma(1+\alpha_x)}. \tag{10}$$

The melting rate for the range $(0, D_{\text{m1}})$ of region (i) is then the difference between the complete integral $(0, \infty)$ and the integral over (D_{m1}, ∞) (also known as the lower incomplete gamma function). Then for region (ii) a similar difference is taken between integrals over (D_{m1}, ∞) and (D_{m2}, ∞), likewise for region (iii). Region (iv) simply integrates on (D_{m3}, ∞). The liquid production in each range (ii)–(iv) is used to find the number of shed drops by dividing by the mass of the corresponding drop size.

For computational efficiency, lookup tables for incomplete gamma functions are generated at the first time step for a range of arguments (e.g., Verlinde et al. 1990; Ferrier 1994; Morrison and Milbrandt 2015) of the function $\Gamma(a + \alpha_x, r)/\Gamma(b + \alpha_x)$, where r is the ratio $D/D_{n,x}$ and a and b are constants particular to each equation. For example, the first numerator term of (10) has $r = D_{\text{m1}}/D_{n,x}$, $a = 2$, $b = 1$, and the second term has the same except $a = 2.5 + b_x$. The lookup tables have a range of r from 0 to 100 and α from $\alpha_{\min}$ to $\alpha_{\max}$ (i.e., 0 to 15 in this work), with $\Delta r = 1/4$ and $\Delta\alpha = 1/16$. A large value of r generally means the integral is over only the outer tail of the distribution and therefore small. The largest r values result from $D_{\text{m3}}/D_{n,x}$ when the characteristic hail (or graupel) diameter $D_{n,x}$ is small. The division by $\Gamma(b + \alpha_x)$ yields a smoother function than the numerator alone, and thus requires lower resolution for a given interpolation accuracy.

Multimoment bulk schemes, including the NSSL scheme, typically preserve the mean ice particle mass during melting by calculating the ice particle number loss rate as the simple division of the mass melting rate by the current mean particle mass, i.e., $N_{\text{melt}} = q_{\text{melt}}(N/q)$ (e.g., Ziegler 1985; Zrnić et al. 1993; Ferrier 1994). This is a reasonable strategy in a two-moment scheme but has the effect of removing a fraction of both large and small ice particles because the distribution shape stays constant. The three-moment framework allows the calculation of both the complete melting of small particles and the partial melting and shedding from large particles. This can change the mean particle mass depending on the ratio of the number concentration loss (from whole particle melting at $0 < D \le D_{\text{m1}}$) to the total mass loss. For example, small mean-mass hail can increase in mean diameter as the smallest particles are removed. If the mean-mass hail size is large (i.e., sufficiently larger than D_{m1}) with a narrower spectrum, then concentration loss is minimal and the mean size shrinks.

The number loss from ice melting in the size range 0 to D_{m1} is treated as complete melting of a fraction of particles at each diameter (see appendix A) as

$$\left.\frac{dN_x}{dt}\right|_{D_{\text{m1}}} = \int_0^{D_{m1}} \frac{1}{m_x(D)} \frac{\partial m_x(D)}{\partial t} n_x(D)\, dD. \tag{11}$$

Substituting using Eq. (3) and integrating yields

$$\left.\frac{dN_x}{dt}\right|_{D_{\text{m1}}} = -\frac{N_x}{c_x D_{n,x}^2} f_{\text{mlt}} \text{nvent}_{D_1}, \tag{12}$$

where

$$\text{nvent}_{D_1} = \frac{1}{\Gamma(1+\alpha_x)} \{c_1[\gamma^*(-1+\alpha_x, D_{\text{m1}}/D_{n,x})] + c_2 \text{Sc}^{1/3}(a_x\gamma/\nu)^{1/2} D_{n,x}^{(1+b_x)/2} [\gamma^*(-1/2+\alpha_x + b_x/2, D_{\text{m1}}/D_{n,x})]\}, \tag{13}$$

and $\gamma^*(x, y)$ is the lower incomplete gamma function.[2] Note that nvent_{D_1} is invalid for $\alpha \le 1$ and becomes large as $\alpha \to 1$. Thus, an alternate approximation is calculated for $\alpha \le 1.5$ by subdividing the diameter range $[0, D_1]$ into two or more size ranges or "bins." The mass melting rate in each bin is calculated as above and then divided by the average particle mass for the bin to derive the number loss rate. The bin average particle mass is the ratio of total bin mass to total bin number, as calculated using incomplete gamma functions. A simple three-bin calculation (0–1.5, 1.5–4.5, and 4.5–9.0 mm) yields sufficient accuracy compared to four to six bins. As will be seen in the results, the shape parameter can quickly exceed 1.5 as melting begins, so the alternate calculation is generally confined to the top of the melting layer.

The strategy of whole particle melting attempts to preserve the net number of particles of a given mass, but this has a side effect on the resulting spectrum of small ice particles because liquid fraction is not tracked here. For example, if one begins with N ice particles with mass m_0, at a later time (under the

[1] $\Gamma(x, y) = \int_y^{\infty} t^{x-1} e^{-t}\, dt$.

[2] $\gamma^*(x, y) \equiv \Gamma(x) - \Gamma(x, y)$.

effect of melting only) there will still be N particles of the same mass, having melted by some fraction f. Here, the particles are represented as fN raindrops and $(1 - f)N$ unmelted ice particles. In reality, of course, there are N particles with ice cores of mass $(1 - f)m_0$, so this method misrepresents this ice mass as the equivalent number of unmelted particles. In the Takahashi bin scheme, this means that ice particles with $D < D_{m1}$ only reach the surface by surviving through the whole melting layer. Particles that start with $D > D_{m1}$ can shrink until they become "stuck" at $D = D_{m1}$, so that ice at $D < D_{m1}$ does not necessarily represent a natural ice spectrum. These particles can be thought of as representing the remaining total ice mass in mixed phase particles that would contain smaller ice cores, which could be tracked with an additional variable to the model to track the amount of liquid that develops on the ice as it melts (e.g., Phillips et al. 2007).

The integrated reflectivity change for whole particle melting (w.p.mlt; appendix A) across the entire spectrum is

$$\left.\frac{\partial Z_x}{\partial t}\right|_{\text{w.p.mlt}} = \int_0^\infty \frac{D^3}{c_x}\frac{\partial m_x(D)}{\partial t} n_x(D)\, dD \tag{14}$$

$$= -\frac{N_x D_{n,x}^4}{c_x} f_{\text{mlt}} \text{zvent}, \tag{15}$$

where

$$\text{zvent} = \frac{1}{\Gamma(1+\alpha_x)}\left[c_1\Gamma(5+\alpha_x) + c_2\Gamma\left(\frac{11}{2}+\alpha_x+\frac{b_x}{2}\right)\text{Sc}^{1/3}(a_x\gamma/\nu)^{1/2} D_{n,x}^{(1+b_x)/2}\right]. \tag{16}$$

Because shedding induces twice the reflectivity change of ice as fractional whole particle loss (appendix A), (14) is integrated over the limits (D_{m1}, ∞) to get the rate for shedding particles, which yields the same form as (15), with the replacement of zvent by zvent_{D1} and the introduction of the upper incomplete gamma function:

$$\text{zvent}_{D1} = \frac{1}{\Gamma(1+\alpha)}\left[c_1\Gamma\left(5+\alpha_x, \frac{D_{m1}}{D_{n,x}}\right) + c_2\Gamma\left(\frac{11}{2}+\alpha_x+\frac{b_x}{2}, \frac{D_{m1}}{D_{n,x}}\right)\text{Sc}^{1/3}(a_x\gamma/\nu)^{1/2} D_{n,x}^{(1+b_x)/2}\right]. \tag{17}$$

Again, the reflectivity rate for the range $(0, D_{m1})$ is found by subtraction. The hail Z rate for shedding over (D_{m1}, ∞) is simply twice the whole particle melting rate for the same interval.

If the number loss by melting is greater than the control–bulkcontrol–bulk amount, the mean particle mass increases since the total mass loss is the same in both methods (for the same starting PSD). This generally forces the shape parameter to increase, depending on the reflectivity loss. The value of α (of any species) is limited to a maximum value of $\alpha_{\max} = 15$ for process rate equations, both for numerical and practical reasons: certain terms become very large but ratios change slowly, such that allowing larger values has diminishing returns. The moments are allowed to evolve such that the actual shape parameter may exceed $\alpha_{\max}$, but the calculated value is simply capped (appendix C), and moments are not scaled or adjusted to force the actual shape parameter to be consistent with this limit. Thus, to prevent the new melting scheme (bin–bulk) from trying to narrow the hail distribution beyond $\alpha_{\max}$, the N and Z tendencies are switched to the original control–bulk scheme when the shape parameter exceeds a threshold of $\alpha_{\text{mxmlt}} = 14.5$. (The mass tendency remains the same regardless of α_x.) Note that the rain moment tendencies are still calculated with the new method, and only the graupel and hail tendencies are directly affected by α_{mxmlt}. Currently, α is also limited to a minimum value of 0, but slightly negative values (i.e., $\alpha > -1$) are physically valid and may be allowed in future work.

A sophisticated three-moment hail scheme was also developed by Loftus et al. (2014) that is in some ways comparable to the one presented here, and each of the parameterizations has unique features. The Loftus hail includes prediction of liquid water fraction retained on hail particles (via the total heat content), whereas the NSSL scheme used here assumes that all liquid is immediately shed. [An experimental version of the NSSL scheme with an explicit water fraction prediction has been developed by Silveira (2016) that follows Ferrier (1994).] In the Loftus scheme, liquid is shed as 1-mm drops from larger ($D \geq 9$ mm) hail particles (with the amount based on lookup tables), but the reflectivity change in hail is assumed not to affect the shape parameter. Very small ice particles that can melt in one time step are transferred to rain in the Loftus parameterization, but partial melting of larger hail particles contributes to the liquid fraction and are retained. Thus, the Loftus scheme may have less direct impact on the shape parameter due to melting, but this is not clear.

Other spectral bin schemes have also implemented parameterizations of Rasmussen et al. (1984). Phillips et al. (2007) incorporated the results into the two-dimensional Hebrew University Cloud Model (HUCM; Khain and Sednev 1995), but the maximum hail diameter in that scheme was smaller than 9 mm diameter, so no shedding effects were possible from large hail. More recently, Kacan and Lebo (2019) presented an updated spectral scheme with predicted liquid fraction of mixed-phase hydrometeors, with maximum hail diameter around 10 cm.

A hybrid-bin version of hail melting was also set up to check consistency with the bin-emulating equations. Here, the hybrid bin is applied only for melting of graupel and hail, which are converted to bin distributions to calculate rates. Hydrometeors are otherwise kept in bulk form (moments only) for all other processes (e.g., advection, turbulent mixing). The bulk hail DSD was discretized within the microphysics routine using the same mass grid and calculations as in the Takahashi bin scheme. The bin calculations produced resulting spectra of hail and rain, which were transformed into bulk rates for number, mass, and reflectivity. The hybrid results agreed very well with the bin–bulk results and thus are not shown.

3. 1D steady hail shaft

a. Setup

This first set of tests uses a 1D framework similar to the pure sedimentation experiments of Milbrandt and Yau (2005a),

Mansell (2010), and Dawson et al. (2014). The sedimentation results of Loftus et al. (2014) and Dawson et al. (2014) both included melting in differing frameworks. Loftus et al. (2014) took the common approach of releasing a single pulse of ice particles, which convolves the time-dependent behavior of both melting and transient size sorting. Dawson et al. (2014) set a constant source of ice particles that eventually reached a steady-state solution, which is revisited later in section 5. In the 1D hail shaft, we take this latter approach of a constant hail source, but with no source-relative horizontal wind (i.e., zero winds), which at steady state has no wind-induced size sorting and focuses on the effects of melting alone.

As in Dawson et al. (2014), an imposed size distribution of hail is maintained at the top of the domain and allowed to fall and melt until a steady-state profile is reached (30 min). Deposition and evaporation are disabled, and the thermodynamic profile is maintained as a constant background state (i.e., no feedback from microphysics). The hail has a fixed density of 900 kg m^{-3} and initial $\alpha_h = 2$. In the small hail case, the mean-mass diameter is 3 mm and mixing ratio is 6 g kg^{-1}, and for the larger hail case they are 15 mm and 0.5 g kg^{-1}, respectively. An additional test with 15-mm hail uses an initial $\alpha_h = 8$. The vertical grid has 32 levels with constant grid spacing of 200 m for a depth of 6400 m, and the time step is 5 s. The profile is a southern plains supercell storm environment (Calhoun et al. 2014) with surface and top temperatures of 30.3° and −14.7°C, with the 0°C level at about 4400 m (Fig. 2).

b. *Small 3-mm hail*

For hail starting with a mean-mass diameter of 3 mm, the control–bulk, bin–bulk, and spectral bin melting results have similar profiles of mass content and reflectivity (Figs. 3a,d,g), indicating that the melting rates are quite comparable across the three schemes. Hail mass content (e.g., at 1 km altitude) and hail reflectivity (e.g., at the ground) for bin–bulk, however, show a better match to the bin result. Hail reflectivity in bin–bulk is about 12 dBZ higher at the ground than in control–bulk. The more dramatic change is in the hail-shape parameter (Figs. 3b,e,h), where bin–bulk quickly increases to α_{mxmlt}, similar to the bin result. Bin–bulk maintains higher hail reflectivity by having higher mean-mass diameter and mass content than control–bulk (cf. Figs. 3c,f), although these are slightly offset by the higher shape parameter. It should be noted that control bulk has slightly greater melting rates than the others because it includes a contribution from rain collection, which is neglected by bin–bulk and bin. If the rain collection is also neglected in control–bulk, the hail mass content and reflectivity increase slightly (Fig. 3a), while the shape parameter and diameters decrease slightly (Figs. 3b,c) because of slightly decreased melting-induced size sorting, as discussed below.

Raindrop sizes are comparable in both bulk schemes because the hail diameters are small enough that drop production is dominated by the 0 to D_{m1} portion of the hail spectrum. At the top of the melting layer (2.5–3.5 km), bin–bulk has smaller rain diameters from the assumed complete melting of smaller ice particles (Figs. 3c,f), which is also seen in the bin result (Fig. 3i). If rain size sorting is disabled, the diameter profile remains nearly unchanged for bin–bulk (not shown), which indicates that it is primarily driven by the size of melting ice. The bin scheme was run without drop–drop interactions for a fairer comparison with the bulk schemes, but Figs. 3h and 3i have additional raindrop profiles with collection and collisional breakup turned on. The drop interactions produce small breakup fragments that result in a lower mean drop diameter and push the rain shape parameter toward zero.

Further comparison is given by the hail particle size distributions (PSDs) at the surface in Fig. 4a. The bin scheme result has larger numbers in the tail than the equivalent gamma function fit. The thick tail is partly an artifact of nonconservation of reflectivity in a spectral scheme that predicts only one variable (particle number) per bin. When mass is lost by shedding, the shrinking particle becomes split between its current and the next smaller bin, which preserves number and mass but not necessarily reflectivity. Khain et al. (2008) developed an extra constraint for the reflectivity, which has been applied in Fig. 4a as the "Z-cons" plots. The reflectivity constraint does shrink the tail, but can cause negative values, which have been filled by borrowing mass from neighboring bins. (This causes the zero bin value at 0.013 m in Fig. 4a.) The result is better reflectivity conservation at the cost of small departures from number conservation, while mass is still conserved precisely. The gamma distributions for both bin results are quite close to each other, with Z-cons being slightly narrower mainly because of its slightly lower reflectivity moment. Both of the bulk scheme PSDs have obvious differences from the bin gamma fits, but bin–bulk sees a better match to the bin-fit gamma distribution at the larger diameters. Relatively poor agreement is expected at smaller diameters since the bin scheme can completely remove smaller particles and here has zero particles for $D < 2.1$ mm (because small ice cannot shrink). The gamma fits for the bin results have shape parameters of 29 or higher, which is much larger than the limit of 15 in the bulk scheme. Nevertheless, the larger value of α in bin–bulk does reduce the number of tiny particles compared to control–bulk.

c. *Sensitivity to D_{m1}*

Variation of the nonshedding/shedding threshold diameter D_{m1} has direct consequences on the hail diameter, as shown in Fig. 5 for both the bin–bulk and bin schemes. A lower value of D_{m1} (e.g., 7 mm) in the hail-shaft experiment reduces the net number concentration loss, which leads to smaller final hail diameters (i.e., less increase of the mean diameter). The smaller D_{m1} causes an increase in shedding and therefore reflectivity loss, such that the maximum shape parameter is reached at a higher altitude (corresponding to the inflection point in the diameter profile in bin–bulk). Likewise, an increase of D_{m1} (e.g., from 9 to 11 mm) allows a larger increase in hail mean diameter via the greater loss of number by whole particle melting. In terms of the melting rates, D_{m1} shifts the ratio of melted mass between small ($D \leq D_{\text{m1}}$) and large ($D > D_{\text{m1}}$) particles as well as the proportional change in number concentration. These perturbations to D_{m1} have little to no effect on the rain diameter in the 3-mm hail case (not shown). Similar small shifts are also seen for the 15-mm hail tests with

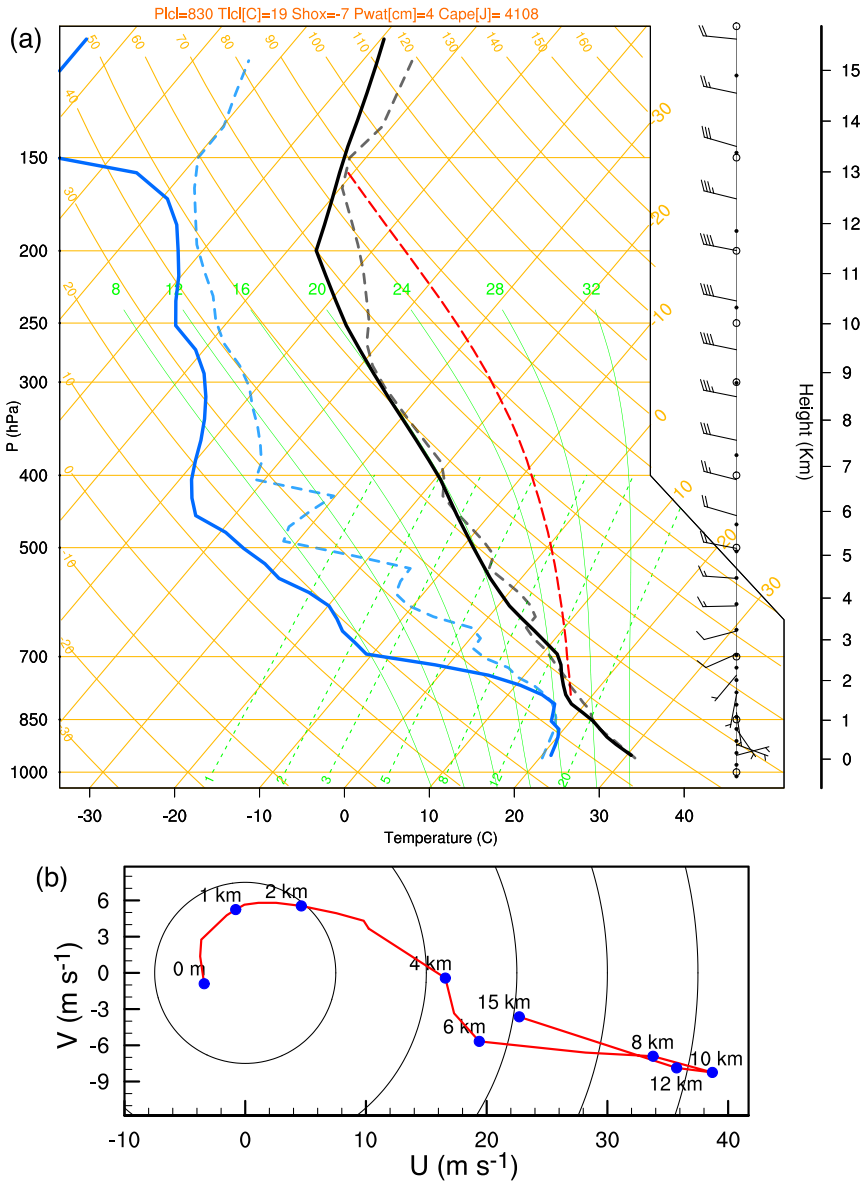

FIG. 2. (a) Skew T–log$p$ soundings for 3D simulations of 1 Jun 2008 (solid) and 1D hail shaft (dashed). (b) Hodograph for the 1 Jun 2008 at the model levels. [Slight differences from Dawson et al. (2014) are a result of sampling at different model levels.]

bin–bulk, and only very small changes in the bin scheme as a larger majority of ice mass is carried in sizes larger than 11 mm.

d. Size sorting induced by melting

In Figs. 3b and 3c the control–bulk shape parameter and mean-mass hail diameter $\overline{D}_h$ can be seen to increase toward the surface, even though the number loss rate by melting does not directly change the mean hail diameter. The maximum mass diameter D_{MxMas} (equivalent to the area-weighted diameter) follows the same pattern, and is shown because it is sensitive to α and gets closer to $\overline{D}_h$ when α is large. This is also seen in bin–bulk below the level where α_{mxmlt} is reached and reflectivity and number rates are reverted to the same method as control–bulk. Figure 3e has an additional curve for $\alpha_{\mathrm{mxmlt}} = 12$, which shows the continued increase in α at the same rate as in Fig. 3b. What explains this behavior? The answer is that melting removes mass and thus induces size sorting, much like a source-relative horizontal wind. Without any melting or other mass loss, the steady-state sedimentation fluxes become balanced, and the hail size and shape parameter become constant with height, as seen in Fig. 6.

Gravitational size sorting can be disabled by using only the mass-weighted fall speed for sedimentation of all moments (N, q, and Z), for example as done in Dawson et al. (2014).

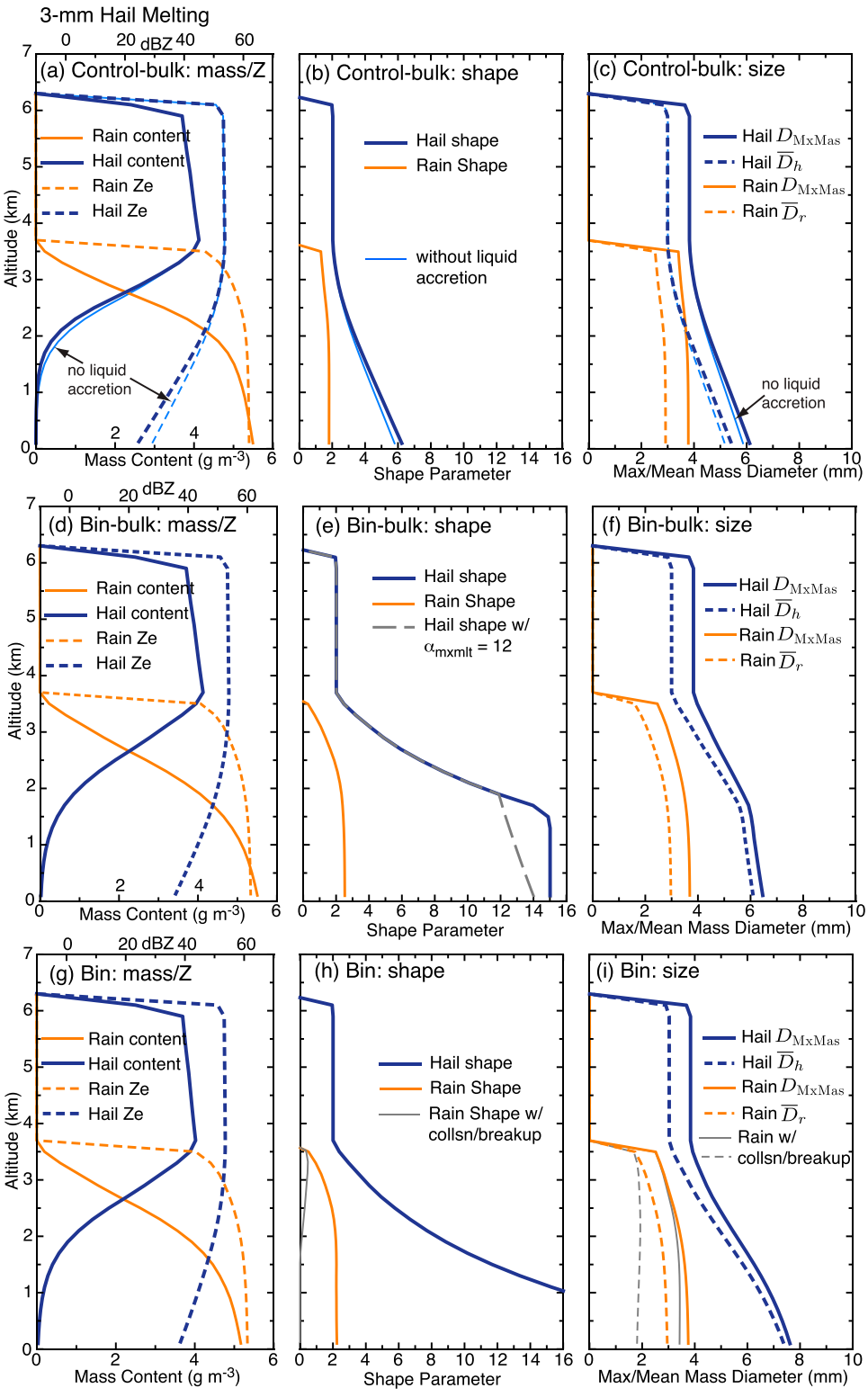

FIG. 3. Steady-state hail and rain profiles with 3-mm hail constantly released at 6.1-km altitude for (a)–(c) control–bulk, (d)–(f) bin–bulk, and (g)–(i) bin schemes. Variables are (left) mass content and reflectivity, (center) spectrum shape parameter (predicted or fitted value), and (right) mean-mass and maximum-mass (i.e., area-weighted) diameters. Also shown in (a)–(c) are the slight changes in hail when liquid accretion is neglected from the melting rate. In (e), the $\alpha_{mxmlt} = 12$ curve illustrates the continued increase of α from size sorting alone. Also (h) and (i) indicate the changes in rain when collisional breakup is allowed.

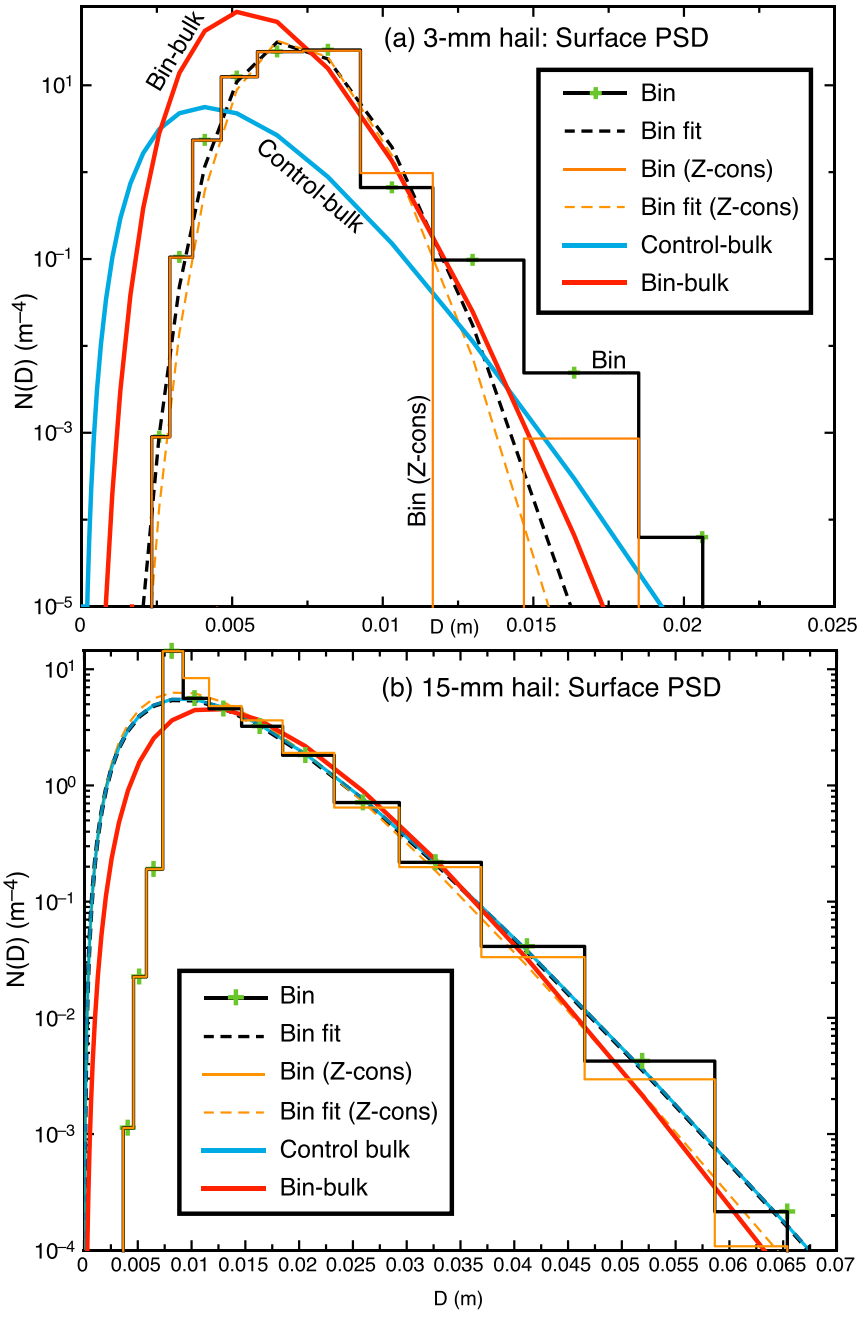

FIG. 4. Hail particle size distributions (PSD) at the lowest model level at steady state for (a) 3- and (b) 15-mm starting mean diameters. The Z-cons bin model variant applies a constraint to conserve the reflectivity moment.

For control–bulk, the hail shape and diameter again become constant as in the no-melting case (Figs. 7b,c). When gravitational size sorting is disabled in the bin–bulk parameterization, however, the effects on the shape parameter and hail size are still quite similar (Figs. 7e,f) as with sorting. The rate of increase in shape parameter is slightly less without size sorting, as would be expected. The test with $\alpha_{\mathrm{mxmlt}} = 12$ also shows that size sorting was responsible for the continued increase in hail size below 1.5 km altitude. Whether or not the melting-induced size sorting is considered physical, it at least has the correct effect for small hail. For a three-moment scheme, size sorting is automatically controlled by feedback through an increasing shape parameter. In a two-moment scheme with a small shape parameter (e.g., $\alpha = 0$), however, melting may lead to or exacerbate excessive size sorting unless some correction is applied. If a liquid fraction on ice were predicted (e.g., Ferrier 1994;

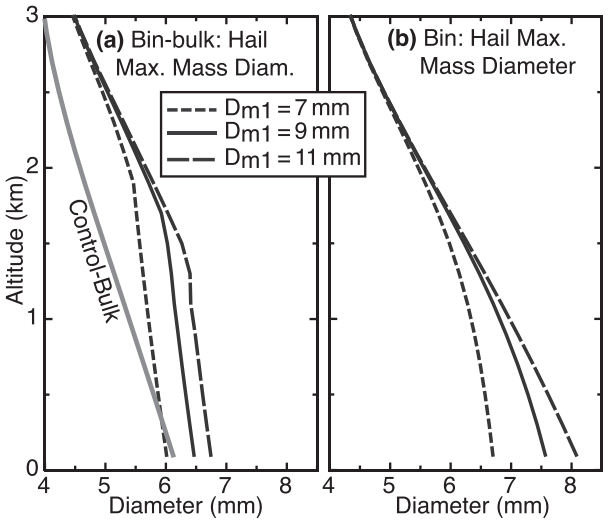

FIG. 5. Hail maximum mass diameter for different values of D_{m1} for (a) bin–bulk and (b) bin. As in Fig. 3, the initial hail mean diameter is 3 mm, and the default D_{m1} is 9 mm. The control–bulk result is shown in (a) for reference.

Loftus et al. 2014; Silveira 2016; Cholette et al. 2019), then the size sorting effect could be lessened by the retention of more mass within the ice category.

e. Large 15-mm hail

In contrast to the 3-mm hail results, the bulk schemes have hail characteristics for the 15-mm hail case (Figs. 8a–f) that are more similar to each other as well as to the bin scheme (Figs. 8g–i). The hail PSDs at the lowest model level (Fig. 4b) show mostly minor differences. Here again the Z-cons constraint on the bin scheme results in a slightly narrower distribution (reduced number of larger particles) and better agreement with the bin–bulk PSD. It is again obvious that the gamma function fit does not represent the small end of the spectrum where the bin scheme can completely remove small particles (although this is partly unrealistic, as noted above). A bulk scheme always has small numbers of small ice within the distribution, so the continuous removal of small particles in bin–bulk may be responsible for the slightly greater mean hail diameter compared to the bin result (Figs. 8f,i).

The bin scheme hail spectra in Fig. 4b exhibit a steep drop-off in number for diameters less than the peak value at about 8 mm, which is similar to the best-sampled (i.e., largest number of hailstones) case in Ziegler et al. (1983, their collection case "B"). Collection B occurred within a hail core (C. Ziegler 2019, personal communication), which suggests that storm-relative winds perhaps played a lesser role in sorting out smaller stones. The peak in Fig. 4b at 9 mm arises from the shrinking particles becoming "stuck" at this size, as noted in section 2. In nature, the ice cores would continue to melt within a liquid shell, but with the same total particle mass. This would reduce and shift the peak in $N(D)$ in terms of ice cores, and there would still be a peak of same-mass mixed-phase particles (except for collisions causing breakup of the liquid portion). We speculate that the slope would still be fairly steep, as these particles still represent the total ice mass for $D < D_{m1}$ but would be spread out to smaller sizes.

The major difference between the bulk schemes for the 15-mm hail is seen in the rain reflectivity and diameter, as well as the rain shape parameter (Figs. 8a–f). The rain diameters of bin–bulk are a good match to the bin scheme (Figs. 8f,i), although rain content is slightly lower in bin–bulk (Figs. 8d,g). Control bulk, on the other hand, produces large raindrops with greater total reflectivity than the others. This results from a simplistic conversion, where raindrop masses are set equal the mean ice particle mass or the prescribed maximum

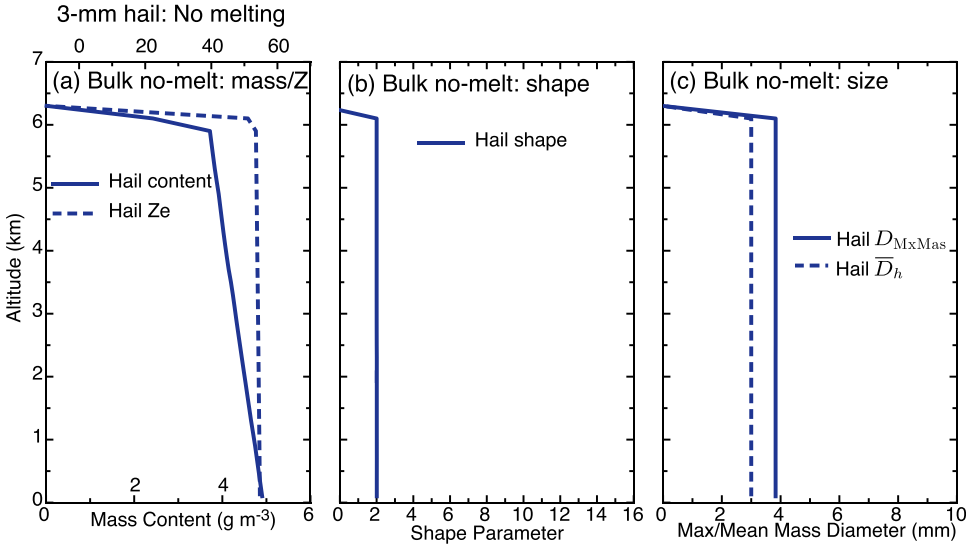

FIG. 6. Steady-state (bulk scheme at 30 min) profile with 3-mm hail constantly released at 6.1-km altitude, but with melting disabled (i.e., pure sedimentation). Results are essentially identical for the bin scheme (not shown).

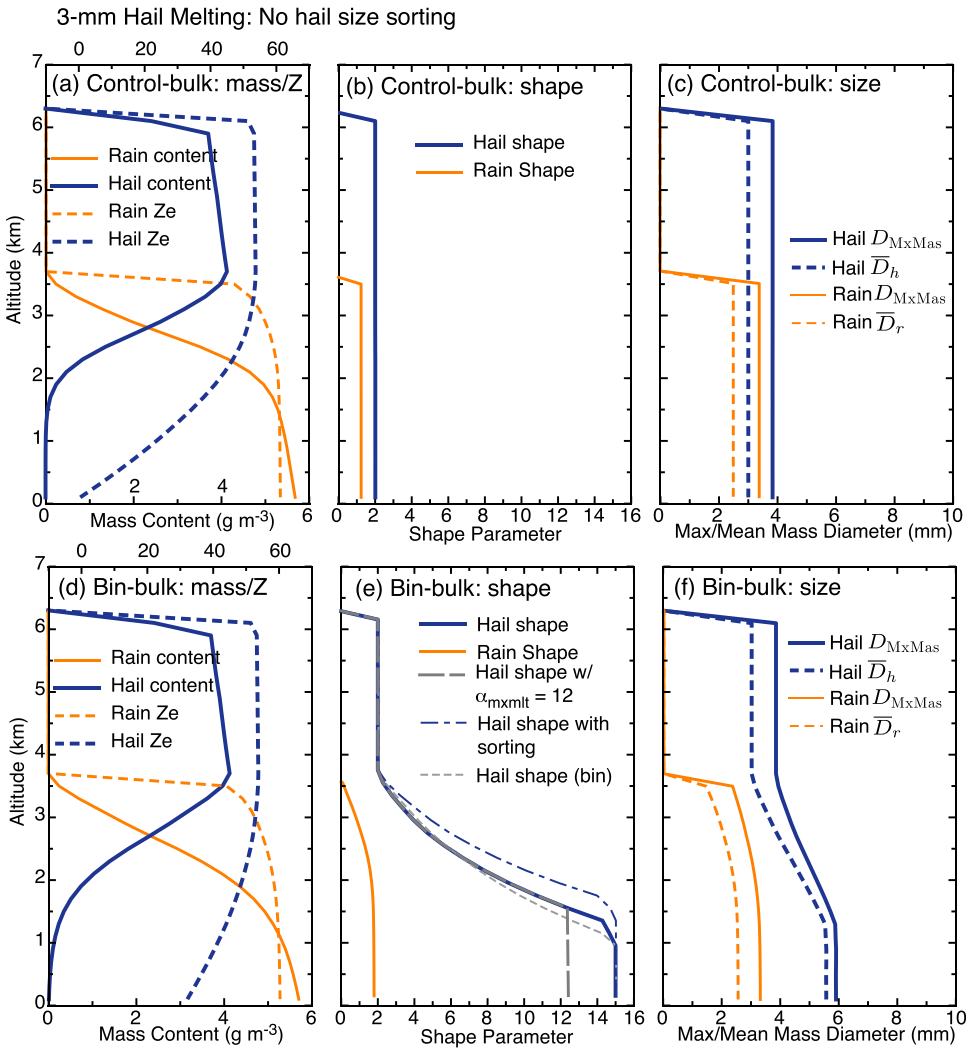

FIG. 7. Steady-state profile with 3-mm hail as in Fig. 3, but with size sorting of hail disabled for (a)–(c) control–bulk and (d)–(f) bin–bulk. For comparison, (e) repeats the shape parameter plots from Figs. 3e and 3h for bin–bulk and bin.

mass-weighted rain diameter (6 mm here), whichever is smaller. Thus, the melting in control–bulk is producing only large drops, which also results in larger rain reflectivity (Fig. 8b) and a narrow size distribution (i.e., large shape parameter; Fig. 8b). For control–bulk, an alternate rain size parameterization ("Alt-Rain") was implemented that improved the rain characteristics somewhat. This Alt-Rain approach uses the maximum mass (i.e., area-weighted) hail diameter D_{MxMas} to select a single melting regime in Fig. 1. For $D_{\mathrm{MxMas}} \leq D_{\mathrm{m1}}$ (complete melting), the rain size is again set by the mean hail mass, but for $D_{\mathrm{MxMas}} > D_{\mathrm{m1}}$ the single corresponding shed drop size is used to set the diameter of the new raindrops (i.e., 4.5, 3, or 1.5 mm). In the 3-mm hail case, the alternate rain size has negligible effect because the hail maximum mass diameter is within the complete melting regime. At diameters less than about D_{m2}, however, it still predicts excessive rain diameters because it does not account for the substantial contribution of smaller shed drops at $D > D_{\mathrm{m2}}$, as will be seen in the following section.

Another aspect of the new melting scheme is that the mean hail size can be decreased when melting is dominated by particles with $D > D_{\mathrm{m1}}$. This can occur with sufficiently large mean hail diameter and shape parameter. As a demonstration, the 15-mm hail shaft was repeated with the initial shape parameter increased from 2 to 8. Figure 9 overlays the mean hail diameters for control–bulk, bin–bulk, and bin for comparison. Bin–bulk and bin show a reduction in mean hail size toward the ground, which is the physically correct behavior for a narrow distribution of large ice particles. Control–bulk, on the other hand, sees a slight increase in diameter that is caused by the melting-induced size sorting.

4. Supercell simulation

a. Setup

The second group of tests compares simulations of the 1 June 2008 supercell thunderstorm case that was used in

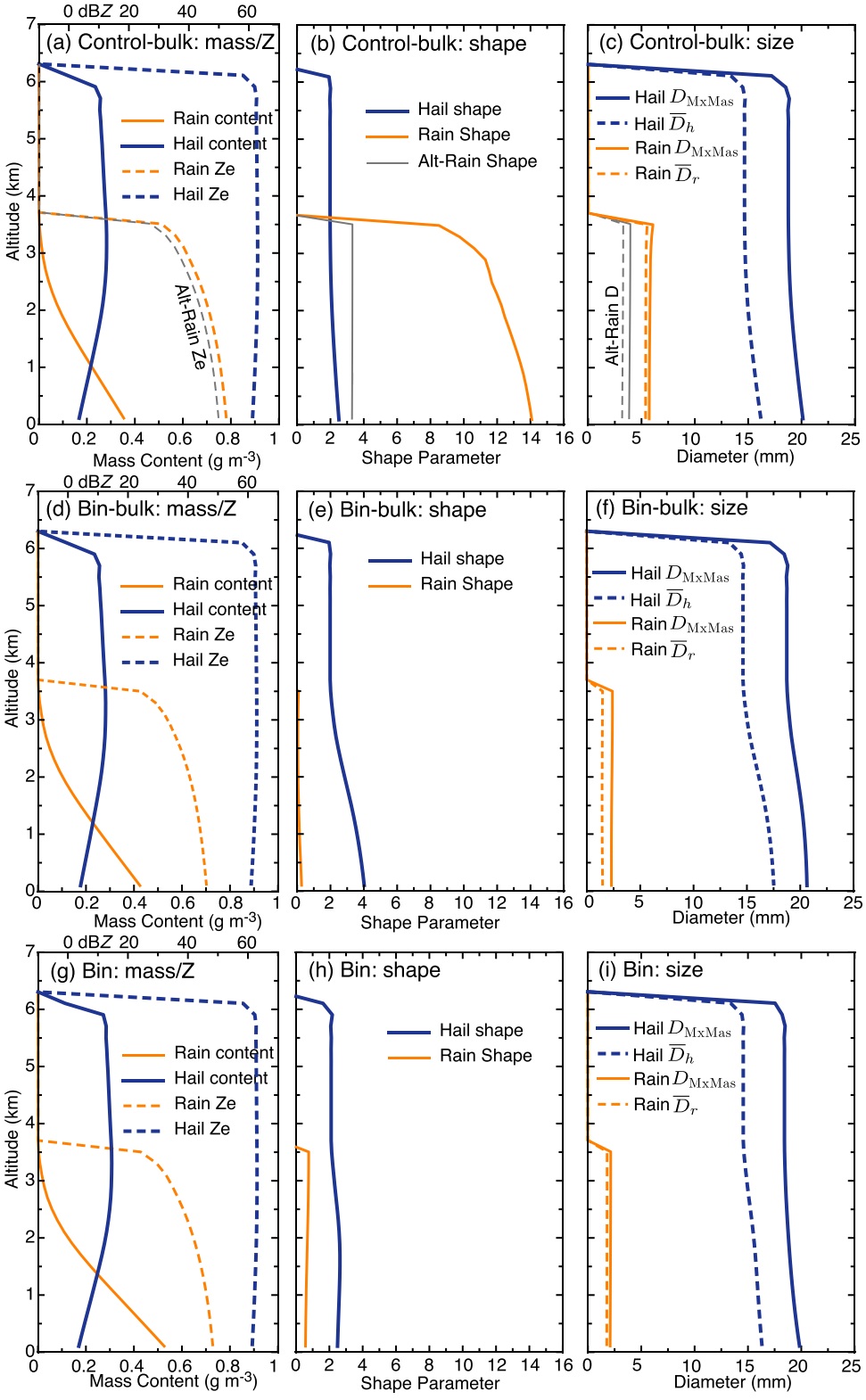

FIG. 8. Steady-state profiles as in Fig. 3, but with 15-mm hail constantly released at 6.1-km altitude for (a)–(c) control–bulk, (d)–(f) bin–bulk, and (g)–(i) bin schemes. Control–bulk in (a)–(c) includes rain profiles for the alternate shedding scheme (Alt-Rain) based on hail maximum-mass diameter.

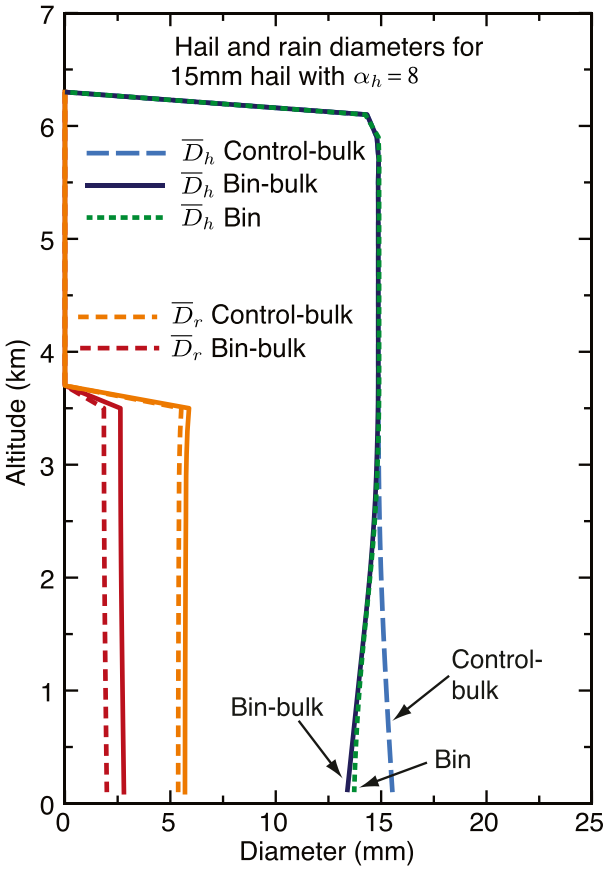

FIG. 9. Size profiles of hail and rain when hail has an initial mean size of 15 mm and shape parameter $\alpha_h = 8$ instead of $\alpha_h = 2$. Rain diameters from the Takahashi bin are similar to the bin–bulk result (not shown).

Dawson et al. (2014), and the initial model profile is shown in Fig. 2. This nontornadic hailstorm occurred in northwest Oklahoma and had clear hail signatures in the dual-polarization radar data (Kumjian et al. 2010) that were compared with model simulations by Dawson et al. (2014). Our focus here is mainly to compare the control–bulk and bin–bulk melting results, with the bin scheme added to assess consistency with bin–bulk. The horizontal domain was 100 km × 100 km with a grid spacing of 500 m. The model depth was 20 km with stretched vertical spacing (50 levels), starting with 200 m at the lowest level and increasing by about 3.5% per level up to a maximum of 500 m at about 9-km altitude. The concentration of cloud condensation nuclei was set as a function of height $\{1000[\rho_{air}(z)/\rho_0]\ \text{cm}^{-3}\}$ for both the bulk and bin schemes. The Takahashi bin microphysics used the continental size spectrum (Takahashi 1978) for nucleated cloud droplets, which is somewhat narrower than the assumed droplet distribution in the NSSL bulk scheme.

Convection was initiated by a combination of thermal perturbation and updraft forcing via an acceleration term (Mansell et al. 2010). A spheroidal region (radii of 15 and 3 km) was centered at 3-km altitude with a maximum temperature perturbation of 3 K, and water vapor was added to maintain the original relative humidity. A spheroidal region of acceleration forcing was used to simulate convergence in the boundary layer, with a central value of 0.12 m s^{-2}. The forcing was horizontally centered at the thermal location, but set at 1.7-km altitude with radii of 10 and 1.5 km. The forcing region had a grid-relative motion of -1.67 m s^{-1} westward and 6.67 m s^{-1} northward, which was estimated from the initial storm motion. The forcing was maintained for the first 40 min of simulation.

b. *Supercell results*

Simulations of the 1 June 2008 supercell storm show features among the melting schemes that are analogous to the hail-shaft examples. The simulated reflectivities in Fig. 10 (at 70 min) are calculated by a T-matrix-based S-band radar emulator (Jung et al. 2008; Dawson et al. 2014) with a setting that all ice particles are considered to have dry surfaces because it does not currently support a wet surface for the Takahashi bin microphysics. At 70 min, there are minimal reflectivity differences between the bulk schemes (Figs. 10a,c), and they generally match the radar observations of a strong reflectivity forward flank (Dawson et al. 2014). The Takahashi bin reflectivity (Fig. 10e) compares less well, having weaker values in the right (south) flank of the core and slightly higher values in the left (northern) flank, but still has recognizable supercell characteristics. The control–bulk rain median volume diameter D_{0r} values (Fig. 10b) are excessively large in the reflectivity core region where larger graupel and hail are melting, even when the Alt-Rain method is applied (Fig. 10b inset). The small drop shedding from larger hail in bin–bulk and bin (Figs. 10d,f), on the other hand, results in similar patterns of maximum D_{0r} in the transition region from larger to smaller melting ice. The three simulations all have quite comparable patterns of D_{0r} farther out (north and east) in the forward flank region (i.e., outside of the main core).

The rain diameters in bin–bulk, although less excessive than control bulk, may still be too big. Disdrometer measurements from supercell storms presented by Friedrich et al. (2013) suggest that values of D_{0r} larger than 5 mm would be quite rare, but also difficult to sample adequately. Drop size measurements at the ground also have various uncertainties, but it seems likely that collisional or other breakup could be important. The bin scheme here does include collisional breakup and shows consistently lower D_{0r} than bin–bulk, but this could also be related to lower precipitation rate and lower simulated reflectivity. A test with the bin scheme in which collisional breakup was turned off yielded substantially similar results (not shown), suggesting that breakup is less important.

The hail shape parameters in Fig. 11 echo the 1D examples: Control–bulk has the lowest values (widest distributions), whereas bin–bulk and bin exhibit similar patterns, but with higher values in bin–bulk (similar to Figs. 8b,e,h), which could be related to poor representation of the gamma function fits for the bin scheme PSDs. The vertical cross sections for bin–bulk and bin (Figs. 11d,f) exhibit melting features over a continuum of hail sizes (larger at $X = 35$–45 km to smaller at $X = 70$ km, as shown in Fig. 12). The smaller ice particles melt more rapidly with height (slower fall speeds) and more quickly reach larger shape parameter values. Both of the bulk schemes have a

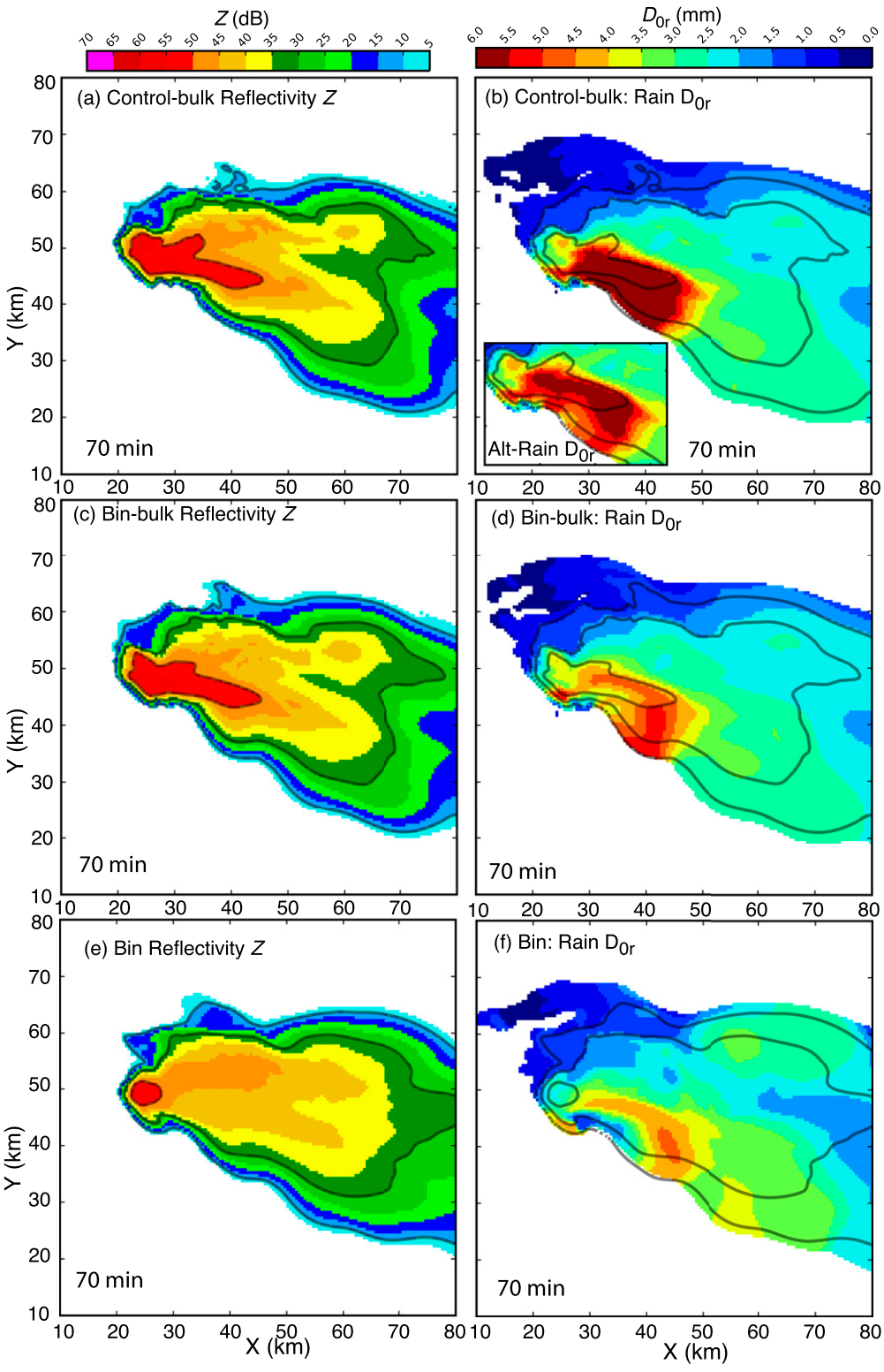

FIG. 10. Simulated (left) radar reflectivity Z_H and (right) rain median volume diameter D_{0r} of the 1 Jun 2008 supercell for (a),(b) control, (c),(d) new bin-emulating melting, and (e),(f) spectral bin microphysics at 0.93 km AGL. All panels include simulated Z line contours at 10, 30, and 50 dBZ.

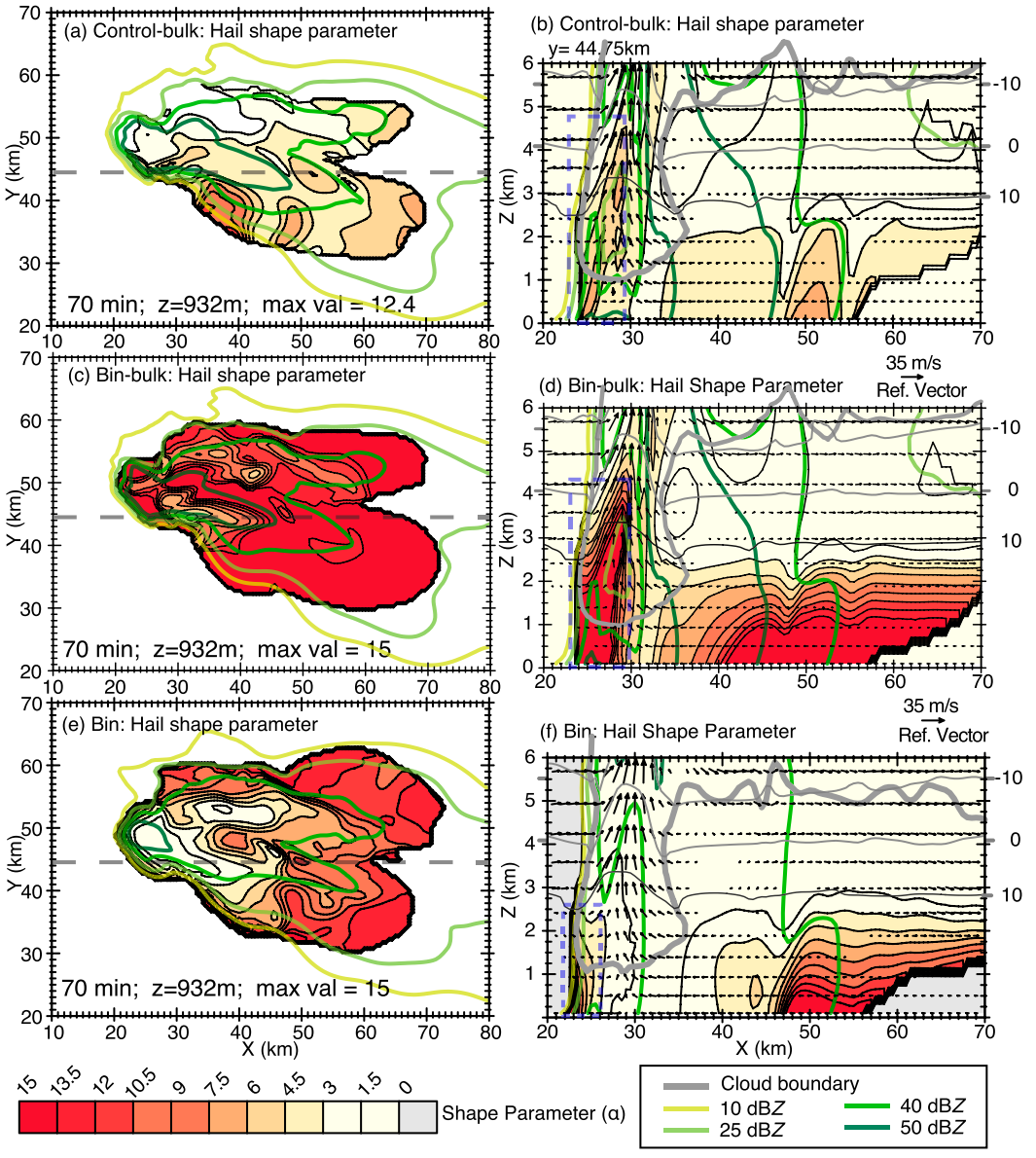

FIG. 11. Hail shape parameters (α, color fill) for simulations of 1 Jun 2008 for (a),(b) control–bulk, (c),(d) bin–bulk, and (e),(f) spectral bin microphysics. (left) Horizontal cross sections at 0.93 km AGL. (right) Vertical cross section at $Y = 44.75$ km as indicated by dashed lines in (a), (c), and (e). Line contours of reflectivity are as noted in the legend. In (b), (d), and (f), the dashed box indicates the column of larger shape parameters.

prominent column (up to 5 km) of high shape parameters on the back (west) side of the updraft (Figs. 11b,d, dashed box area), and this feature is clearly enhanced by melting in bin–bulk. The bin scheme has a shorter, narrower feature (Fig. 11f), but it does have a similar distinct hail shaft on the west side of the bounded weak-echo region as in the bulk results (not shown).

Hail diameters shown in Fig. 12 roughly follow expectations from the 1D hail-shaft examples, although independently evolving 3D wind and microphysical fields complicate the comparisons. The bin–bulk D_{MxMas} values (Fig. 12b) are generally larger than control–bulk (Fig. 12a) near and outside the 50-dBZ contour, where sizes are about 8 mm or smaller. In the higher reflectivity core, however, control–bulk diameters are larger, which is a combination of similar, though slightly larger, mean-mass diameter (not shown) along with lower shape parameter values (Figs. 11a,c). The high shape parameters in bin–bulk likely help to limit further diameter increases when the mean diameters exceed about 9 mm, as seen in the 1D tests. The 3D sedimentation example in the following section shows the hail shrinking effect in a more controlled manner. For the bin scheme, Fig. 12c shows mean diameter D_h rather than D_{MxMas} because the PSD generally consists of small numbers of larger particles. Some very

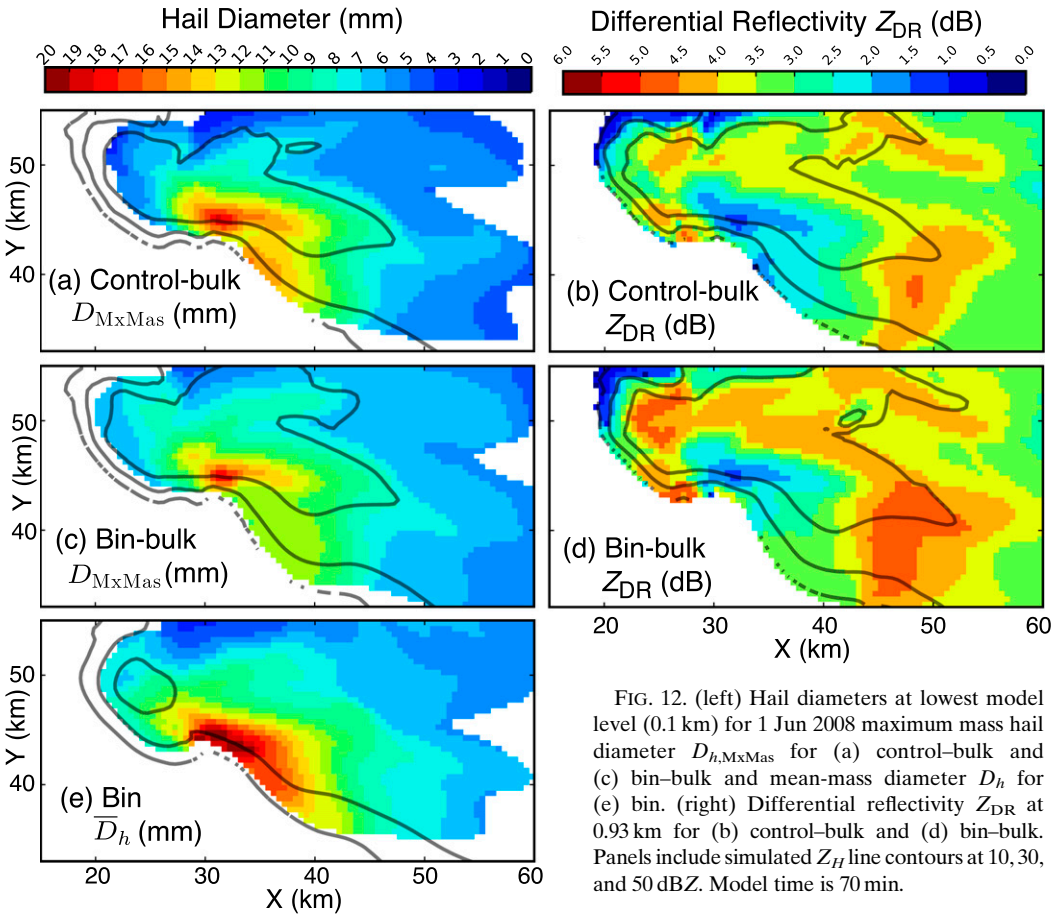

FIG. 12. (left) Hail diameters at lowest model level (0.1 km) for 1 Jun 2008 maximum mass hail diameter $D_{h,\mathrm{MxMas}}$ for (a) control–bulk and (c) bin–bulk and mean-mass diameter D_h for (e) bin. (right) Differential reflectivity Z_{DR} at 0.93 km for (b) control–bulk and (d) bin–bulk. Panels include simulated Z_H line contours at 10, 30, and 50 dBZ. Model time is 70 min.

small numbers of larger bin diameters may be numerically valid but are not necessarily physically meaningful, and even less so when weighted by area or mass. Outside of the core of large diameters, the bin and bin–bulk schemes agree fairly well given the differences in reflectivity. All three simulations consistently place the largest hail on the southern edge of the storm along or near the 30-dBZ contour.

The emulated differential reflectivity Z_{DR} fields in the bulk schemes (Figs. 12b,d) have similar structures as the simulations in Dawson et al. (2014) for the same case with an earlier version of the NSSL three-moment scheme. As in Dawson et al. (2014), the hail is allowed to have a wet surface for calculating Z_{DR}: At points where hail and rain are both present, part of the rain mass is transferred to the hail as a diagnosed liquid fraction. This option has not been developed for the Takahashi bin scheme, thus no comparable field is shown. Control–bulk and bin–bulk have very similar Z_{DR} patterns, but bin–bulk has higher values outside of the hail core. This is a result of slightly increased hail diameters, that, when assumed to be water coated, can act like large raindrops. The low Z_{DR} in the hail core for both bulk results is an indication that the hail dominates the emulated signal such that the very different rain D_{0r} in the two schemes (Figs. 10b,d) has little influence.

5. 3D steady-state hail shaft

a. Setup

The third and final set of simulations examines the hail and rain size differences seen in the supercell simulations with control–bulk and bin–bulk, but without the complication of storm evolution. This also provides a follow-up on the three-dimensional sedimentation experiments of Dawson et al. (2014). They examined the effects of the same 1 June 2008 wind profile (Fig. 2) on a steady-state hail shaft, finding that hail size sorting was crucial for the formation of a pronounced Z_{DR} (differential reflectivity) radar signature. As in Dawson et al. (2014), a constant size distribution of hail is imposed in a circular area (radius of 3 km) at the top of the domain (12 km) and allowed to fall and melt until a steady-state profile is reached (40 min). The hail has a fixed density of 900 kg m^{-3} (i.e., not variable), initial shape parameter of 0, mean-mass diameter of 4 mm, and a mixing ratio of 5 g kg^{-1} at the center of the circle and tapering to zero at the edge via a cosine-squared function. The wind fields are held constant by turning off all momentum tendencies. The time step is 5 s as in the 1D hail shafts.

b. Results

The surface fields for the control–bulk result in Fig. 13 closely match the patterns in corresponding figures in Dawson et al. (2014), including the band of higher Z_{DR} values that wrap

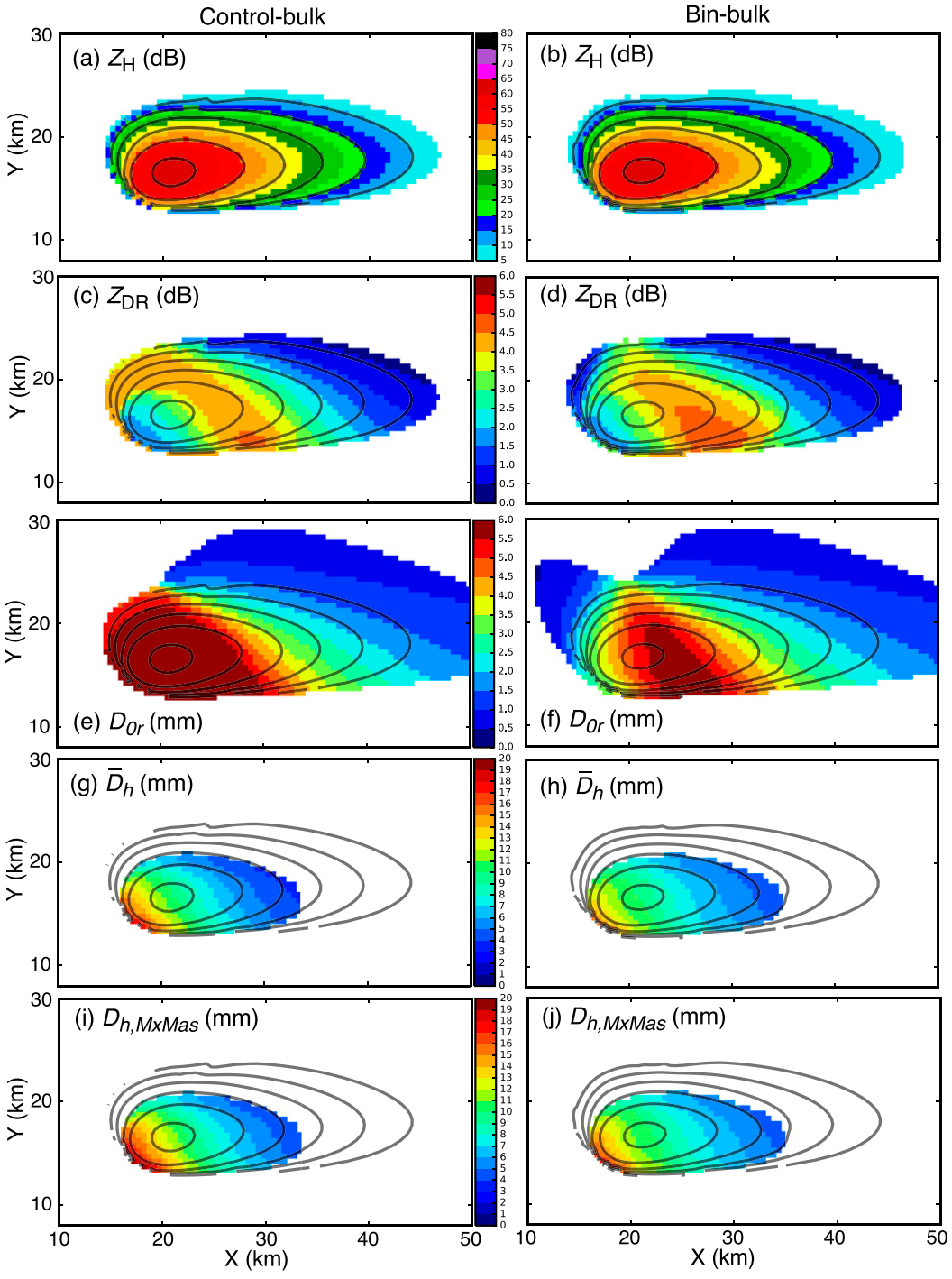

FIG. 13. 3D steady-state hail shafts using the 1 Jun 2008 sounding and either the (left) control–bulk or (right) bin–bulk microphysics at 100-m altitude. A constant hail source is set at 12-km altitude. Fields shown are (a),(b) simulated radar reflectivity Z_H, (c),(d) differential reflectivity Z_{DR}, (e),(f) rain median volume diameter D_{0r}, and (g),(h) maximum-mass hail diameter $D_{h,MxMas}$. Panels include simulated Z_H line contours at 10–50 dBZ in intervals of 10 dBZ.

counterclockwise into the northwest edge of reflectivity (Fig. 13e). Also notable are the large rain median volume diameters D_{0r} [instead of mean diameter in Dawson et al. (2014)] in the southwest quadrant coincident with larger hail and low Z_{DR}. As noted above for the supercell result, the low Z_{DR} region in the southwest results from large hail despite the large drop diameters that would otherwise promote higher Z_{DR}. The base reflectivity fields for control–bulk and bin–bulk are nearly

indistinguishable (Figs. 13a,b), but in bin–bulk the Z_{DR} band is cut off from the northwest. The D_{0r} pattern in bin–bulk (Fig. 13f) implies that smaller drops from shedding hail are reducing the Z_{DR} in the northwest section. The result again highlights ambiguities of interpretation when the radar signal is dominated by one hydrometeor type that masks the returns from others.

The hail mean-mass diameters in Figs. 13g and 13h are similar to each other, but in bin–bulk the values are slightly increased to the east of the reflectivity core, as in the supercell result (Fig. 12). Additionally, the maximum values of D_h at the southwest edge in bin–bulk are slightly smaller. This occurs because they are in the regime of large diameter coupled with high α_h, as seen in Fig. 9 for the 1D hail shaft, that leads to reduction of D_h. Larger values of D_h actually occur at higher points along the fall trajectories (not shown), which is consistent with melting dominated by $D > D_{m1}$. The maximum-mass diameters in Figs. 13i and 13j take α_h into account, as well, such that the differences east of the core are reduced by lower shape values in control bulk ($\alpha_h \sim 7$–10) compared to bin–bulk ($\alpha_h = 15$). Both bulk schemes have more similar α_h (6–10) on the west side of the core, such that the diameter differences are roughly the same as for D_h.

The differences seen in D_{0r} and $D_{h,\mathrm{MxMas}}$ patterns parallel the full simulation results in Figs. 10b,d and 12a,b, respectively. The rain median volume diameters have strong reductions in bin–bulk where the hail sizes are large and favor the shedding of smaller drops. Bin–bulk shows slightly enhanced $D_{h,\mathrm{MxMas}}$ (by roughly 1 mm) compared to control–bulk in the regions downshear of the main reflectivity core, where values are generally smaller than about 9 mm. In and near the core, however, bin–bulk shows lower hail diameter than control–bulk, which can be attributed to reduced number concentration loss at larger hail size and shape parameter.

6. Conclusions

An application of the Rasmussen et al. (1984) hail melting and shedding results has been implemented in both a three-moment bulk ice scheme and a spectral bin microphysics scheme, with similar realistic physical effects produced in both. The modified bulk NSSL scheme (bin–bulk) was set up to emulate the bin method by integrating melting rates over discrete size ranges that have particular characteristics of shedding (different drop sizes produced) or not shedding at all (at smaller hail diameters). Melting causes the mean ice diameter to increase and the spectral shape to narrow in both the bin and bin–bulk schemes when the hail spectrum is wide or hail diameter not too large. For large mean diameter and narrow size spectrum, the bin and bin–bulk schemes correctly reduce the mean hail diameter. The unmodified bulk scheme (control–bulk), however, always increases the hail size through induced gravitational size sorting. The resulting rain sizes in the modified schemes are strongly affected by the melting process when a substantial fraction of the melting is at ice sizes ($D >$ 9 mm) that shed smaller drops. It turns out that the effects of larger hail on the rain DSD via small drop shedding may be more substantial than hail size effects, considering the very minor changes in reflectivity compared to large effect on rain size in the supercell and 3D hail-shaft simulations. This suggests that a two-moment scheme could also benefit just from an improved treatment of shed drop size.

A secondary highlight of these results is the explicit recognition that melting induces size sorting in a bulk microphysics scheme, whether three moment or two moment, by maintaining a leading edge type of profile. Any substantial removal of mass as a function of height in the column would have a similar effect. The mass loss rates effectively define a size-sorting profile in a steady-state hail shaft, and the induced sorting is analogous to the effects of source-relative horizontal wind (Kumjian and Ryzhkov 2012; Dawson et al. 2014, 2015). In a two- or three-moment scheme, this can have the correct *effect* to increase mean hail diameter (except for larger, narrower hail spectra), though perhaps for a physically incorrect (or unintentional) *reason*. Excessive size sorting is generally recognized as a potential problem in two-moment schemes for fast-falling hydrometeors, but rapid melting of slower-falling snow may also adversely affect ice size via induced sorting. In the 1D test with 3-mm hail, there is a suggestion of a similar, but opposite, effect on rain from having source terms as function of height that emulates a ''trailing tail'' phenomenon that tends to reduce the mean particle size just below the melting level. Other physics that are neglected, however, may mask this effect. One approach to mitigate either effect is to track the liquid fraction on ice so that less (or no) mass is removed from the ice category. Last, while polarimetric radar has provided many insights to storm microphysics, ambiguities still remain, particularly for particles that contribute weakly to the signal. In situ observations are thus still crucial for evaluating model results.

Acknowledgments. The simulations were made possible through computing resources provided by NOAA (HPC ''Jet''). The authors are indebted to Tsutomu Takahashi for his contribution of the spectral bin microphysics code. We thank Jacob Carlin for valuable feedback on the manuscript. Suggestions from Jason Milbrandt and two anonymous reviewers resulted in numerous improvements in both clarity and content.

APPENDIX A

Reflectivity Rate from Melting

Given a population of N ice particles of diameter D and particle mass m (and total mass $M = Nm$), the effect of differential melting can be considered in two approaches, where the total mass melting rate is Ndm/dt. One approach is to remove the same mass dm/dt from all particles of that size (i.e., shrink all particles), as would be appropriate for sufficiently large ice particles that shed most of the meltwater. In this case $dN/dt = 0$. Smaller ice particles ($D < 9$ mm), however, do not shed but gradually develop liquid water shell around an ice core (e.g., Rasmussen et al. 1984). If liquid fraction on ice is not predicted, the second approach is to emulate this process by removing a fraction of whole particles to account for the melting, such that $dN/dt = (dM/dt)/m$, and the ice particles lose number but do not change size. As noted in the main text, this

is a trade-off which preserves the number of particles of a given mass but does not allow small ice cores to shrink.

Starting with reflectivity as simply D^6,

$$Z(D) = n(D)D^6. \tag{A1}$$

Differentiation of (A1) produces two terms:

$$\frac{\partial Z(D)}{\partial t} = \frac{\partial n(D)}{\partial t}D^6 + 6n(D)\frac{\partial D}{\partial t}D^5. \tag{A2}$$

The first term on the right-hand side represents smaller particles ($D \le D_{\text{crit}}$) that melt completely (i.e., do not shed, with a change in particle number but not radius), and the second term is for larger particles ($D > D_{\text{crit}}$) that partially melt and shed off mass (with a change in radius but not particle number). Thus, for a given hail (or graupel) size, only one term will be nonzero:

$$\left.\frac{\partial Z(D)}{\partial t}\right|_{D\le D_{\text{crit}}} = \frac{\partial n(D)}{\partial t}D^6, \tag{A3}$$

$$\left.\frac{\partial Z(D)}{\partial t}\right|_{D> D_{\text{crit}}} = 6n(D)\frac{\partial D}{\partial t}D^5. \tag{A4}$$

Since the parameterization used here does not treat mixed-phase particles (i.e., does not track liquid on ice), we take the total melting rate of small particles $\partial M/\partial t$ and transform the number rate using $\partial n(D)/\partial t = [\partial n(D)/\partial m]\partial m/\partial t = [n(D)/m]\partial m/\partial t$, so that (A3) becomes

$$\left.\frac{\partial Z(D)}{\partial t}\right|_{D\le D_{\text{crit}}} = \frac{n(D)D^6}{m}\frac{\partial m(D)}{\partial t} \tag{A5}$$

$$= \frac{n(D)D^{6-d_x}}{c_x}\frac{\partial m(D)}{\partial t}, \tag{A6}$$

where mass m has been replaced by using mass–diameter relationship $m = c_x D^{d_x}$.

The same mass–diameter relationship can then be used to substitute the diameter time derivative for a mass derivative in (A4):

$$\frac{\partial m}{\partial t} = c_x d_x D^{d_x-1}\frac{\partial D}{\partial t}. \tag{A7}$$

And then substitute for $\partial D/\partial t$ for large particles:

$$\left.\frac{\partial Z(D)}{\partial t}\right|_{D> D_{\text{crit}}} = 6n(D)\frac{D^{5-(d_x-1)}}{c_x d_x}\frac{\partial m(D)}{\partial t}. \tag{A8}$$

And by setting $d_x = 3$ and $c_x = (\pi/6)\rho_x$, the equations become

$$\left.\frac{\partial Z(D)}{\partial t}\right|_{D\le D_{\text{crit}}} = n(D)\frac{D^3}{c_x}\frac{\partial m(D)}{\partial t}, \tag{A9}$$

$$\left.\frac{\partial Z(D)}{\partial t}\right|_{D> D_{\text{crit}}} = 2n(D)\frac{D^3}{c_x}\frac{\partial m(D)}{\partial t}. \tag{A10}$$

Thus, there is a factor-of-2 difference between treating the melting as removing whole particles compared to particles shedding off the meltwater and becoming smaller.

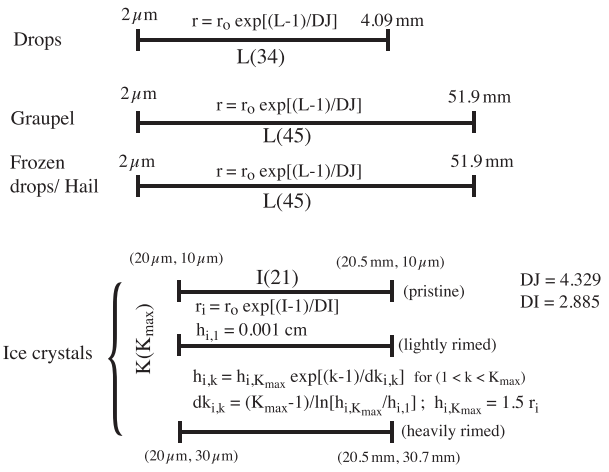

FIG. B1. Hydrometeor classifications in the updated Takahashi spectral bin scheme, adapted from Takahashi (1976a). Size bins are exponential in particle radius, with drops, graupel, and hail starting at $r_0 = 2\,\mu$m, up to 34 bins for drops and 45 for graupel/hail. Ice crystals grow in radius (21 bins, from 20 μm to 20.5 mm) and thickness ($K_{\max} = 5$, from 10 μm to $1.5r_i$).

APPENDIX B

Updates to Takahashi Spectral Bin Microphysics

The spectral bin microphysics were adapted from the version used in Takahashi and Shimura (2004), which closely followed Takahashi (1976b,a, 1983). The bin categories are summarized in Fig. B1. The number of rain size bins was changed from 33 to 34, which increased the maximum radius from 3.2 to 4.1 mm. A main modification was the addition of incremental melting of graupel, hail, and ice crystals. A number of further changes were made to the bin scheme to align the physical parameterizations with the NSSL bulk scheme, for example in particle terminal fall speeds, ice crystal nucleation, and drop freezing, as noted below. Formulations of saturation pressures and temperature-dependent latent heating rates were also implemented to be consistent with the bulk scheme.

a. Ice crystals

Ice crystal characteristics are retained from Takahashi (1976a) with a D^2 dependence for mass that is consistent with observations of snow (e.g., Cox 1988; Brandes et al. 2007; Szyrmer and Zawadski 2010). Ice crystal fall speeds use the same fit of data from Jayaweera and Cottis (1969) for the relationship between the Reynolds number (Re) and the Best (or Davies) number (Be) for disks

$$\text{Re}_{\text{crystal}} = \exp[0.65\log(\text{Be}) - 1.38], \tag{B1}$$

where

$$\text{Be} = \frac{2hD^2}{\eta^2}\bar{\rho}_{\text{ice}}\rho_{\text{air}}g \tag{B2}$$

and

$$V_{\text{crystal}} = \frac{\eta\text{Re}}{D\rho_{\text{air}}}. \tag{B3}$$

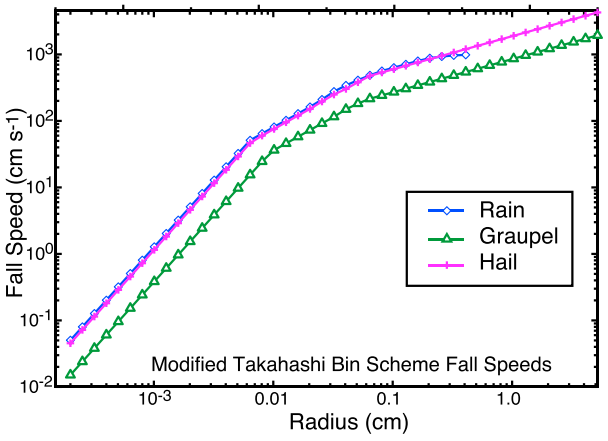

FIG. B2. Hydrometeor fall speeds in the updated Takahashi spectral bin scheme.

All base fall speeds are calculated using sea level air density and then modified by a factor of $\gamma = (\rho_0/\rho_{\rm air})^{0.39}$. The exponent of 0.39 was found by calculating fall speeds at various air densities and finding a best fit. Vapor nucleation of ice crystals and riming ice multiplication follow Mansell et al. (2010).

b. Fall speeds

Rain, graupel, and hail fall speeds are initially calculated as in Takahashi (1976a), Eqs. (10)–(15), with the modification that the conditional particle radii are adjusted for each type to match the intersection points of the curve fits. Instead of testing the value of the Best number, the fall speeds are limited by the formulas used in the bulk scheme (Mansell et al. 2010), which generally applies to particles with diameters larger than 1 mm. Raindrops in the bulk scheme use a fit of the Gunn and Kinzer (1949) data:

$$v_{t,r}(D) = a_r[1 - \exp(-f_r D)], \tag{B4}$$

and graupel and hail use

$$v_{t,x}(D) = \left(\frac{4D\rho_x g}{3C_D\rho_0}\right)^{1/2}, \tag{B5}$$

where the drag coefficient C_D depends on the particle density as in Mansell et al. (2010). The resulting base fall speeds are continuous functions, shown in Fig. B2 for the parameters used in the present study. Rain fall speeds level off at large sizes, which is not captured by the original power law formulation. For the values used here, the hail bin fall speeds were always less than the bulk formulation (by about 10% for $d > 1$ mm) and thus were not affected by (B5).

c. Drop freezing

Spontaneous drop freezing uses the results directly from Bigg (1953), where the critical drop volume as a function of temperature is given by

$$v_{\rm crit} = \exp[16.2 + (T - T_0)]. \tag{B6}$$

Drop freezing by interaction with ice crystals produces frozen drops if $v_{\rm xtal} < v_{\rm drop}$ and $m_{\rm drop} > m_{\rm xtal}/2$ and otherwise results in riming of the crystal.

d. Conversions between graupel and frozen drops/hail

Conversions between the high density ice (frozen drops and hail) and low density ice (graupel) are based on the sustained riming density concept of Ferrier (1994) using a time scale of 120 s. Graupel (g) is converted to frozen drops/hail (h) only under wet growth conditions. The graupel particle number N_g conversion rate is

$$\left.\frac{dN_{g,j}}{dt}\right|_{g\to h} = \frac{1}{\Delta t}\mathrm{Min}\left[\frac{\Delta t}{120}, \frac{\Delta m_{{\rm rime},j}}{m_{g,j}}\right] N_{g,j}, \tag{B7}$$

where $m_{g,i}$ is the particle mass and $\Delta m_{{\rm rime},j}$ is the riming growth rate of the jth graupel bin. Meanwhile, frozen drops/hail in dry growth mode can be converted to graupel when the average rime density, $\rho_{\rm rime}$ is less than 0.5 g cm^{-3}, as

$$\left.\frac{dN_{h,j}}{dt}\right|_{h\to g} = \frac{f_{\rm cnv}}{\Delta t}\mathrm{Min}\left[\frac{\Delta t}{120}, \frac{\Delta m_{{\rm rime},j}}{m_{h,j}}\right] N_{h,j}, \tag{B8}$$

where

$$f_{\rm cnv} = \begin{cases} 1.75 - 2.5(\rho_{\rm rime} + 0.2) & \text{for} \quad 0.1 \le \rho_{\rm rime} < 0.5\ \mathrm{g\,cm^{-3}} \\ 0 & \text{for} \quad \rho_{\rm rime} \ge 0.5\ \mathrm{g\,cm^{-3}} \end{cases}.$$

The condition of wet growth is checked by diagnosing the ice surface temperature (e.g., Nelson 1983; Farley and Orville 1986). Here, the wet growth formulation from Farley and Orville (1986) is used:

$$\left.\frac{dm_j}{dt}\right|_{\rm wet} = \frac{2\pi d_j[-a_h(j)K_a(T - T_0) - a_m(j)\Psi L_v\rho_{\rm air}(q_v - q_{v,s,0})]}{L_f + C_w(T - T_0)} + \frac{dm_{\rm ice}}{dt}\left[1 - \frac{C_i(T - T_0)}{L_f + C_w(T - T_0)}\right], \tag{B9}$$

where $dm_{\rm ice}/dt$ is the ice crystal collection rate. The ice temperature is found by iteration as in Farley and Orville (1986). If the wet growth condition is met, excess water is shed as drops of diameter 1.02 mm (Lesins and List 1986) and the sticking efficiency of ice is set to unity.

e. Melting of ice

The melting rate of graupel and frozen drops/hail again follows Farley and Orville (1986), but currently neglects the contribution of accreted liquid:

$$\left.\frac{dm_j}{dt}\right|_{\rm melt} = -\frac{1}{L_f}2\pi d_j[-a_h(j)K_a(T - T_0) - a_m(j)\Psi L_v\rho_{\rm air}(q_v - q_{v,s,0})]. \tag{B10}$$

In the whole particle melting regime, meltwater from particles of mass $m_{x,k}$ is together converted to the number of drops

with a mass that is the lesser of $m_{x,k}$ and the maximum drop bin mass ($m_{r,l=34}$). When particles are allowed to shed and shrink, ice particles with $d \le D_{\mathrm{m1}}$ are still treated as full particle melting, but particles of size $d > D_{\mathrm{m1}}$ shed meltwater as in Fig. 1.

Ice crystal melting uses the same equation form with the appropriate capacitance (disk) and Reynolds number [Eq. (B1)] for the ventilation coefficients

$$\left.\frac{dm_{i,k}}{dt}\right|_{\mathrm{melt}} = -\frac{1}{L_f} 4 d_{i,k} [-a_h(i,k) K_a (T - T_0) - a_m(i,k) \Psi L_v \rho_{\mathrm{air}} (q_v - q_{v,s,0})]. \tag{B11}$$

f. Ice crystal conversion to graupel

In the original bin scheme, the ice crystals in bin $k = k_{\max}$ were assigned a thickness equal to the particle diameter. Particles that rimed beyond this thickness were then converted to graupel. Since these particles may be considered to be already graupel particles, a refinement here reduces the maximum thickness to $h_{i,5} = 0.75 d_i$, and additional riming then causes conversion to graupel.

g. Collisional drop breakup

Takahashi (1976a) included the spontaneous breakup term of Srivastava (1971), but this by itself may be unrealistic without including some kind of collisional breakup (e.g., McTaggart-Cowan and List 1975; Young 1975). Here, a relatively simple collisional breakup has been implemented that follows Brazier-Smith et al. (1972), Brazier-Smith et al. (1973), and Young (1975). Compared to more complex breakup parameterizations (e.g., Low and List 1982; Straub et al. 2010), this simpler scheme is essentially a failure to coalesce: the two colliding drops are returned with reduced masses, and the lost mass produces three new smaller drops. As in Young (1975), the three satellite drops are assumed to take masses of 1.6%, 11.4%, and 87% of the mass loss from the two original drops (Brazier-Smith et al. 1973). Future updates will consider adding a more complex parameterization. Spontaneous breakup is applied only to drops larger than 6.6 mm diameter (following Young 1975), which affects only the largest rain bin.

The stochastic collection–breakup equation is given as

$$\left.\frac{\partial n(x)}{\partial t}\right|_{\mathrm{coll}} = \frac{1}{2}\int_0^{\infty} n(y) n(x-y) E(y, x-y) K(y, x-y)\, dy - n(x)\int_0^{\infty} n(y) K(x,y)\, dy + \int_0^{\infty} n(m)\, dm \int_0^{m} [1 - E(m,y)] K(m,y) P(x;m,y) n(y)\, dy, \tag{B12}$$

where the first term is the source from coalesced drop pairs (masses y and $x - y$), the second term is the loss resulting from all collisions, and the third term is the source term of fragments produced by breakup collisions. The coalescence efficiency is E, and the breakup efficiency is then $1 - E$. Brazier-Smith et al. (1973) and others have split the second term into separate losses for coalescence and breakup collisions, which effectively normalizes the fragment distribution. This separation is unnecessary, however, if the fragment distribution conserves mass (Feingold et al. 1988), in which case the loss term can simply count all collision pairs. In other words, as long as $E_{\mathrm{coal}} + E_{\mathrm{breakup}} = 1$, the original SCE loss term in the pure coalescence case ($E_{\mathrm{coal}} = 1$) includes all losses. The collision kernel $K(x, y)$ includes the geometric sweep out and the collision efficiency (Ogura and Takahashi 1973; Takahashi 1976b).

APPENDIX C

Shape Parameter Solution Method

Using the gamma size distribution function of diameter, Milbrandt and Yau (2005a) derived a relationship between the moments of mass mixing ratio q, total number concentration N_T, and reflectivity Z:

$$Z_x = \frac{G(\alpha)}{c_x^2} \frac{(\rho_{\mathrm{air}} q_x)^2}{N_{Tx}}, \tag{C1}$$

where c_x is from the mass–diameter relationship, $m_x = c_x D^{d_x}$, and

$$G(\alpha) = \frac{(6+\alpha)(5+\alpha)(4+\alpha)}{(3+\alpha)(2+\alpha)(1+\alpha)}. \tag{C2}$$

Multiplying both sides by $(\alpha + 1)$ and then subtracting 1 isolates α against $(1+\alpha)G(\alpha) = G^*(\alpha)$ in an equation that can be solved iteratively:

$$\alpha_{n+1} = \frac{G^*(\alpha_n)}{c_x^2} \frac{(\rho_{\mathrm{air}} q_x)^2}{N_{Tx} Z_x} - 1. \tag{C3}$$

Here, n is the iteration index, and the starting value of α_0 is default value used in the two-moment scheme (but can be any reasonable value). The new value α_{n+1} goes back into the right-hand side, and iterations continue until the convergence criterion of $|\alpha_{n+1} - \alpha_n| < 0.01$, which almost always occurs before the maximum number of iterations ($n = 10$) is reached. Values are constrained to the range ($\alpha_{\min}$, $\alpha_{\max}$). If the final value is at the lower limit $\alpha_x = \alpha_{\min}$, the true value could actually be $\alpha < \alpha_{\min}$, thus the current parameterization ensures consistency of the moments by recalculating Z_x using $\alpha_{\min}$, q_x, and N_{tx}. No action is taken for $\alpha_x = \alpha_{\max}$. For spectral bin species, the three moments are calculated first by summing the distribution with appropriate coefficients and then used in the iteration of (C3). Irregularities in bin spectra such as bimodal structure or sharp cutoffs will of course affect the goodness (and appropriateness) of the gamma fitting, and more sophisticated techniques are possible that would provide statistical measures of accuracy.

Equation (C3) can also be iterated by a Newton–Raphson method employing the derivative. This was tested for comparison, and it was found that although it requires fewer iterations, the greater computation per iteration makes the cost about the same.

REFERENCES

Balsara, D. S., and C.-W. Shu, 2000: Monotonicity preserving weighted essentially non-oscillatory schemes with increasingly high order of accuracy. *J. Comput. Phys.*, **160**, 405–452, https://doi.org/10.1006/jcph.2000.6443.

Beard, K. V., and H. R. Pruppacher, 1971: A wind tunnel investigation of the rate of evaporation of small water drops falling at terminal velocity in air. *J. Atmos. Sci.*, **28**, 1455–1464, https://doi.org/10.1175/1520-0469(1971)028<1455:AWTIOT>2.0.CO;2.

Bigg, E. K., 1953: The supercooling of water. *Proc. Phys. Soc. London*, **66B**, 688–694, https://doi.org/10.1088/0370-1301/66/8/309.

Brandes, E. A., K. Ikeda, G. Zhang, M. Schönhuber, and R. M. Rasmussen, 2007: A statistical and physical description of hydrometeor distributions in Colorado snowstorms using a video disdrometer. *J. Appl. Meteor. Climatol.*, **46**, 634–650, https://doi.org/10.1175/JAM2489.1.

Brazier-Smith, P. R., S. G. Jennings, and J. Latham, 1972: The interaction of falling water drops: Coalescence. *Proc. Phys. Soc. London*, **326A**, 393–408, https://doi.org/10.1098/rspa.1972.0016.

——, ——, and ——, 1973: Raindrop interactions and rainfall rates within clouds. *Quart. J. Roy. Meteor. Soc.*, **99**, 260–272, https://doi.org/10.1002/qj.49709942005.

Bryan, G. H., and J. M. Fritsch, 2002: A benchmark simulation for moist nonhydrostatic numerical models. *Mon. Wea. Rev.*, **130**, 2917–2928, https://doi.org/10.1175/1520-0493(2002)130<2917:ABSFMN>2.0.CO;2.

Calhoun, K. M., E. R. Mansell, D. R. MacGorman, and D. C. Dowell, 2014: Numerical simulations of lightning and storm charge of the 29–30 May 2004 Geary, Oklahoma, supercell thunderstorm using EnKF mobile radar data assimilation. *Mon. Wea. Rev.*, **142**, 3977–3997, https://doi.org/10.1175/MWR-D-13-00403.1.

Cholette, M., H. Morrison, J. A. Milbrandt, and J. M. Thériault, 2019: Parameterization of the bulk liquid fraction on mixed-phase particles in the predicted particle properties (P3) scheme: Description and idealized simulations. *J. Atmos. Sci.*, **76**, 561–582, https://doi.org/10.1175/JAS-D-18-0278.1.

Clark, A. J., and Coauthors, 2012: An overview of the 2010 Hazardous Weather Testbed Experimental Forecast Program Spring Experiment. *Bull. Amer. Meteor. Soc.*, **93**, 55–74, https://doi.org/10.1175/BAMS-D-11-00040.1.

Coniglio, M. C., D. J. Stensrud, and L. J. Wicker, 2006: Effects of upper-level shear on the structure and maintenance of strong quasi-linear mesoscale convective systems. *J. Atmos. Sci.*, **63**, 1231–1252, https://doi.org/10.1175/JAS3681.1.

Cox, C. P., 1988: Modelling precipitation in frontal bands. *Quart. J. Roy. Meteor. Soc.*, **114**, 115–127, https://doi.org/10.1002/qj.49711447906.

Dawson, D. T., II, L. J. Wicker, E. R. Mansell, Y. Jung, and M. Xue, 2013: Low-level polarimetric radar signatures in EnKF analyses and forecasts of the May 8, 2003 Oklahoma City tornadic supercell: Impact of multimoment microphysics and comparisons with observation. *Adv. Meteor.*, **2013**, 818394, https://doi.org/10.1155/2013/818394.

——, E. R. Mansell, Y. Jung, L. J. Wicker, M. R. Kumjian, and M. Xue, 2014: Low-level Z_{DR} signatures in supercell forward flanks: The role of size sorting and melting of hail. *J. Atmos. Sci.*, **71**, 276–299, https://doi.org/10.1175/JAS-D-13-0118.1.

——, ——, and M. R. Kumjian, 2015: Does wind shear cause hydrometeor size sorting? *J. Atmos. Sci.*, **72**, 340–348, https://doi.org/10.1175/JAS-D-14-0084.1.

Fan, J., and Coauthors, 2017: Cloud-resolving model intercomparison of an MC3E squall line case: Part I—Convective updrafts. *J. Geophys. Res. Atmos.*, **122**, 9351–9378, https://doi.org/10.1002/2017JD026622.

Farley, R. D., and H. D. Orville, 1986: Numerical modeling of hailstorms and hailstone growth. Part I: Preliminary model verification and sensitivity tests. *J. Climate Appl. Meteor.*, **25**, 2014–2035, https://doi.org/10.1175/1520-0450(1986)025<2014:NMOHAH>2.0.CO;2.

Feingold, G., S. Tzivion, and Z. Levin, 1988: Evolution of raindrop spectra. Part I: Solution to the stochastic collection/breakup equation using the method of moments. *J. Atmos. Sci.*, **45**, 3387–3399, https://doi.org/10.1175/1520-0469(1988)045<3387:EORSPI>2.0.CO;2.

——, R. L. Walko, B. Stevens, and W. R. Cotton, 1998: Simulations of marine stratocumulus using a new microphysical parameterization scheme. *Atmos. Res.*, **47–48**, 505–528, https://doi.org/10.1016/S0169-8095(98)00058-1.

Ferrier, B. S., 1994: A double-moment multiple-phase four-class bulk ice scheme. Part I: Description. *J. Atmos. Sci.*, **51**, 249–280, https://doi.org/10.1175/1520-0469(1994)051<0249:ADMMPF>2.0.CO;2.

Friedrich, K., E. A. Kalina, F. J. Masters, and C. R. Lopez, 2013: Drop-size distributions in thunderstorms measured by optical disdrometers during VORTEX2. *Mon. Wea. Rev.*, **141**, 1182–1203, https://doi.org/10.1175/MWR-D-12-00116.1.

Gunn, R., and G. D. Kinzer, 1949: The terminal velocity of fall for water droplets in stagnant air. *J. Meteor.*, **6**, 243–248, https://doi.org/10.1175/1520-0469(1949)006<0243:TTVOFF>2.0.CO;2.

Han, B., and Coauthors, 2019: Cloud-resolving model intercomparison of an MC3E squall line case: Part II. Stratiform precipitation properties. *J. Geophys. Res. Atmos.*, **124**, https://doi.org/10.1029/2018JD029596.

Jayaweera, K. O. L. F., and R. E. Cottis, 1969: Fall velocities of plate-like and columnar ice crystals. *Quart. J. Roy. Meteor. Soc.*, **95**, 703–709, https://doi.org/10.1002/qj.49709540604.

Johnson, D. E., P. K. Wang, and J. M. Straka, 1993: Numerical simulations of the 2 August 1981 CCOPE supercell storm with and without ice microphysics. *J. Appl. Meteor.*, **32**, 745–769, https://doi.org/10.1175/1520-0450(1993)032<0745:NSOTAC>2.0.CO;2.

Johnson, M., Y. Jung, D. T. Dawson II, and M. Xue, 2016: Comparison of simulated polarimetric signatures in idealized supercell storms using two-moment bulk microphysics schemes in WRF. *Mon. Wea. Rev.*, **144**, 971–996, https://doi.org/10.1175/MWR-D-15-0233.1.

Jung, Y., G. Zhang, and M. Xue, 2008: Assimilation of simulated polarimetric radar data for a convective storm using the ensemble Kalman filter. Part I: Observation operators for reflectivity and polarimetric variables. *Mon. Wea. Rev.*, **136**, 2228–2245, https://doi.org/10.1175/2007MWR2083.1.

——, M. Xue, and M. Tong, 2012: Ensemble Kalman filter analyses of the 29–30 May 2004 Oklahoma tornadic thunderstorm using one- and two-moment bulk microphysics schemes, with verification against polarimetric radar data. *Mon. Wea. Rev.*, **140**, 1457–1475, https://doi.org/10.1175/MWR-D-11-00032.1.

Kacan, K. G., and Z. J. Lebo, 2019: Microphysical and dynamical effects of mixed-phase hydrometeors in convective storms using a bin microphysics model: Melting. *Mon. Wea. Rev.*, **147**, 4437–4460, https://doi.org/10.1175/MWR-D-18-0032.1.

Khain, A., and I. L. Sednev, 1995: Simulation of hydrometeor size spectra evolution by water-water, ice-water and ice-ice interactions. *Atmos. Res.*, **36**, 107–138, https://doi.org/10.1016/0169-8095(94)00030-H.

——, N. Benmoshe, and A. Pokrovsky, 2008: Factors determining the impact of aerosols on surface precipitation from clouds: An attempt at classification. *J. Atmos. Sci.*, **65**, 1721–1748, https://doi.org/10.1175/2007JAS2515.1.

——, B. Lynn, and J. Shpund, 2016: High resolution WRF simulations of Hurricane Irene: Sensitivity to aerosols and choice of microphysical schemes. *Atmos. Res.*, **167**, 129–145, https://doi.org/10.1016/J.ATMOSRES.2015.07.014.

Klemp, J. B., and R. B. Wilhelmson, 1978: Simulations of right- and left-moving storms produced through storm splitting. *J. Atmos. Sci.*, **35**, 1097–1110, https://doi.org/10.1175/1520-0469(1978)035<1097:SORALM>2.0.CO;2.

Knight, C. A., and N. C. Knight, 1970: The falling behavior of hailstones. *J. Atmos. Sci.*, **27**, 672–681, https://doi.org/10.1175/1520-0469(1970)027<0672:TFBOH>2.0.CO;2.

Kudzotsa, I., and Coauthors, 2016: Aerosol indirect effects on glaciated clouds. Part I: Model description. *Quart. J. Roy. Meteor. Soc.*, **142**, 1958–1969, https://doi.org/10.1002/qj.2791.

Kumjian, M. R., and A. V. Ryzhkov, 2012: The impact of size sorting on the polarimetric radar variables. *J. Atmos. Sci.*, **69**, 2042–2060, https://doi.org/10.1175/JAS-D-11-0125.1.

——, ——, V. M. Melnikov, and T. J. Schuur, 2010: Rapid-scan super-resolution observations of a cyclic supercell with a dual-polarization WSR-88D. *Mon. Wea. Rev.*, **138**, 3762–3786, https://doi.org/10.1175/2010MWR3322.1.

Lesins, G. B., and R. List, 1986: Sponginess and drop shedding of gyrating hailstones in a pressure-controlled icing wind tunnel. *J. Atmos. Sci.*, **43**, 2813–2825, https://doi.org/10.1175/1520-0469(1986)043<2813:SADSOG>2.0.CO;2.

Loftus, A. M., W. R. Cotton, and G. G. Carrió, 2014: A triple-moment hail bulk microphysics scheme. Part I: Description and initial evaluation. *Atmos. Res.*, **149**, 35–57, https://doi.org/10.1016/j.atmosres.2014.05.013.

Low, T. B., and R. List, 1982: Collision, coalescence and breakup of raindrops. Part II: Parameterization of fragment size distributions. *J. Atmos. Sci.*, **39**, 1607–1619, https://doi.org/10.1175/1520-0469(1982)039<1607:CCABOR>2.0.CO;2.

Mansell, E. R., 2010: On sedimentation and advection in multi-moment bulk microphysics. *J. Atmos. Sci.*, **67**, 3084–3094, https://doi.org/10.1175/2010JAS3341.1.

——, and C. L. Ziegler, 2013: Aerosol effects on simulated storm electrification and precipitation in a two-moment bulk microphysics model. *J. Atmos. Sci.*, **70**, 2032–2050, https://doi.org/10.1175/JAS-D-12-0264.1.

——, ——, and E. C. Bruning, 2010: Simulated electrification of a small thunderstorm with two-moment bulk microphysics. *J. Atmos. Sci.*, **67**, 171–194, https://doi.org/10.1175/2009JAS2965.1.

Mason, B. J., 1956: On the melting of hailstones. *Quart. J. Roy. Meteor. Soc.*, **82**, 209–216, https://doi.org/10.1002/qj.49708235207.

McTaggart-Cowan, J. D., and R. List, 1975: Collision and breakup of water drops at terminal velocity. *J. Atmos. Sci.*, **32**, 1401–1411, https://doi.org/10.1175/1520-0469(1975)032<1401:CABOWD>2.0.CO;2.

Milbrandt, J. A., and M. K. Yau, 2005a: A multimoment bulk microphysics parameterization. Part I: Analysis of the role of the spectral shape parameter. *J. Atmos. Sci.*, **62**, 3051–3064, https://doi.org/10.1175/JAS3534.1.

——, and ——, 2005b: A multimoment bulk microphysics parameterization. Part II: A proposed three-moment closure and scheme description. *J. Atmos. Sci.*, **62**, 3065–3081, https://doi.org/10.1175/JAS3535.1.

——, and ——, 2006: A multimoment bulk microphysics parameterization. Part III: Control simulation of a hailstorm. *J. Atmos. Sci.*, **63**, 3114–3136, https://doi.org/10.1175/JAS3816.1.

——, and R. McTaggert-Cowan, 2010: Sedimentation-induced errors in bulk microphysics schemes. *J. Atmos. Sci.*, **67**, 3931–3948, https://doi.org/10.1175/2010JAS3541.1.

Morrison, H., 2012: On the numerical treatment of hydrometeor sedimentation in bulk and hybrid bulk–bin microphysics schemes. *Mon. Wea. Rev.*, **140**, 1572–1588, https://doi.org/10.1175/MWR-D-11-00140.1.

——, and J. A. Milbrandt, 2015: Parameterization of cloud microphysics based on the prediction of bulk ice particle properties. Part I: Scheme description and idealized tests. *J. Atmos. Sci.*, **72**, 287–311, https://doi.org/10.1175/JAS-D-14-0065.1.

——, ——, G. H. Bryan, K. Ikeda, S. A. Tessendorf, and G. Thompson, 2015: Parameterization of cloud microphysics based on the prediction of bulk ice particle properties. Part II: Case study comparisons with observations and other schemes. *J. Atmos. Sci.*, **72**, 312–339, https://doi.org/10.1175/JAS-D-14-0066.1.

Naumann, A. K., and A. Seifert, 2016: Evolution of the shape of the raindrop size distribution in simulated shallow cumulus. *J. Atmos. Sci.*, **73**, 2279–2297, https://doi.org/10.1175/JAS-D-15-0263.1.

Nelson, S. P., 1983: The influence of storm flow structure on hail growth. *J. Atmos. Sci.*, **40**, 1965–1983, https://doi.org/10.1175/1520-0469(1983)040<1965:TIOSFS>2.0.CO;2.

Ogura, Y., and T. Takahashi, 1973: The development of warm rain in a cumulus model. *J. Atmos. Sci.*, **30**, 262–277, https://doi.org/10.1175/1520-0469(1973)030<0262:TDOWRI>2.0.CO;2.

Paukert, M., J. Fan, P. J. Rasch, H. Morrison, J. A. Milbrandt, J. Shpund, and A. Khain, 2019: Three-moment representation of rain in a bulk microphysics model. *J. Adv. Model. Earth Syst.*, **11**, 257–277, https://doi.org/10.1029/2018MS001512.

Phillips, V. T. J., A. Pokrovsky, and A. Khain, 2007: The influence of time-dependent melting on the dynamics and precipitation production in maritime and continental storm clouds. *J. Atmos. Sci.*, **64**, 338–359, https://doi.org/10.1175/JAS3832.1.

Putnam, B. J., M. Xue, Y. Jung, G. Zhang, and F. Kong, 2017: Simulation of polarimetric radar variables from 2013 CAPS Spring Experiment storm-scale ensemble forecasts and evaluation of microphysics schemes. *Mon. Wea. Rev.*, **145**, 49–73, https://doi.org/10.1175/MWR-D-15-0415.1.

Rasmussen, R. M., V. Levizzani, and H. R. Pruppacher, 1984: A wind tunnel and theoretical study on the melting behavior of atmospheric ice particles: III. Experiment and theory for spherical ice particles of radius. *J. Atmos. Sci.*, **41**, 381–388, https://doi.org/10.1175/1520-0469(1984)041<0381:AWTATS>2.0.CO;2.

Silveira, A., 2016: Charge structure and lightning patterns in a simulated mesoscale convective system. Ph.D. thesis, University of Oklahoma, 136 pp.

Snyder, J. C., H. B. Bluestein, D. T. Dawson II, and Y. Jung, 2017: Simulations of polarimetric, X-band radar signatures in supercells. Part I: Description of experiment and simulated ρ_{hv} rings. *J. Appl. Meteor. Climatol.*, **56**, 1977–1999, https://doi.org/10.1175/JAMC-D-16-0138.1.

Srivastava, R. C., 1971: Size distribution of raindrops generated by their breakup and coalescence. *J. Atmos. Sci.*, **28**, 410–415, https://doi.org/10.1175/1520-0469(1971)028<0410:SDORGB>2.0.CO;2.

Straka, J. M., and E. R. Mansell, 2005: A bulk microphysics parameterization with multiple ice precipitation categories. *J. Appl. Meteor.*, **44**, 445–466, https://doi.org/10.1175/JAM2211.1.

——, M. S. Gilmore, K. M. Kanak, and E. N. Rasmussen, 2005: A comparison of the conservation of number concentration for the continuous collection and vapor diffusion growth equations using one- and two-moment schemes. *J. Appl. Meteor.*, **44**, 1844–1849, https://doi.org/10.1175/JAM2314.1.

Straub, W., K. D. Beheng, A. Seifert, J. Schlottke, and B. Weigand, 2010: Numerical investigation of collision-induced breakup of raindrops. Part II: Parameterizations of coalescence efficiencies and fragment size distributions. *J. Atmos. Sci.*, **67**, 576–588, https://doi.org/10.1175/2009JAS3175.1.

Szyrmer, W., and I. Zawadski, 2010: Snow studies. Part II: Average relationship between mass of snowflakes and their terminal fall velocity. *J. Atmos. Sci.*, **67**, 3319–3335, https://doi.org/10.1175/2010JAS3390.1.

Takahashi, T., 1976a: Hail in an axisymmetric cloud model. *J. Atmos. Sci.*, **33**, 1579–1601, https://doi.org/10.1175/1520-0469(1976)033<1579:HIAACM>2.0.CO;2.

——, 1976b: Warm rain, giant nuclei and chemical balance—A numerical model. *J. Atmos. Sci.*, **33**, 269–286, https://doi.org/10.1175/1520-0469(1976)033<0269:WRGNAC>2.0.CO;2.

——, 1978: Precipitation mechanisms in a shallow convective cloud model. *J. Atmos. Sci.*, **35**, 277–283, https://doi.org/10.1175/1520-0469(1978)035<0277:PMIASC>2.0.CO;2.

——, 1983: Numerical simulation of winter cumulus electrification. Part I: Shallow cloud. *J. Atmos. Sci.*, **40**, 1257–1280, https://doi.org/10.1175/1520-0469(1983)040<1257:ANSOWC>2.0.CO;2.

——, and K. Shimura, 2004: Tropical rain characteristics and microphysics in a three-dimensional cloud model. *J. Atmos. Sci.*, **61**, 2817–2845, https://doi.org/10.1175/JAS-3294.1.

Verlinde, J., P. J. Flatau, and W. R. Cotton, 1990: Analytical solutions to the collection growth equation: Comparison with approximate methods and application to cloud microphysics parameterization schemes. *J. Atmos. Sci.*, **47**, 2871–2880, https://doi.org/10.1175/1520-0469(1990)047<2871:ASTTCG>2.0.CO;2.

Wicker, L. J., and R. B. Wilhelmson, 1995: Simulation and analysis of tornado development and decay within a three-dimensional supercell thunderstorm. *J. Atmos. Sci.*, **52**, 2675–2703, https://doi.org/10.1175/1520-0469(1995)052<2675:SAAOTD>2.0.CO;2.

——, and W. C. Skamarock, 2002: Time-splitting methods for elastic models using forward time schemes. *Mon. Wea. Rev.*, **130**, 2088–2097, https://doi.org/10.1175/1520-0493(2002)130<2088:TSMFEM>2.0.CO;2.

Wisner, C., H. D. Orville, and C. Meyers, 1972: A numerical model of a hail-bearing cloud. *J. Atmos. Sci.*, **29**, 1160–1181, https://doi.org/10.1175/1520-0469(1972)029<1160:ANMOAH>2.0.CO;2.

Xue, L., and Coauthors, 2017: Idealized simulations of a squall line from the MC3E field campaign applying three bin microphysics schemes: Dynamic and thermodynamic structure. *Mon. Wea. Rev.*, **145**, 4789–4812, https://doi.org/10.1175/MWR-D-16-0385.1.

Young, K. C., 1975: The evolution of drop spectra due to condensation, coalescence, and breakup. *J. Atmos. Sci.*, **32**, 965–973, https://doi.org/10.1175/1520-0469(1975)032<0965:TEODSD>2.0.CO;2.

Ziegler, C. L., 1985: Retrieval of thermal and microphysical variables in observed convective storms. Part I: Model development and preliminary testing. *J. Atmos. Sci.*, **42**, 1487–1509, https://doi.org/10.1175/1520-0469(1985)042<1487:ROTAMV>2.0.CO;2.

——, P. S. Ray, and N. C. Knight, 1983: Hail growth in an Oklahoma multicell storm. *J. Atmos. Sci.*, **40**, 1768–1791, https://doi.org/10.1175/1520-0469(1983)040<1768:HGIAOM>2.0.CO;2.

Zrnić, D. S., N. Balakrishnan, C. L. Ziegler, V. N. Bringi, K. Aydin, and T. Matejka, 1993: Polarimetric signatures in the stratiform region of a mesoscale convective system. *J. Appl. Meteor.*, **32**, 678–693, https://doi.org/10.1175/1520-0450(1993)032<0678:PSITSR>2.0.CO;2.